
PROTON SPIN-LATTICE RELAXATION IN COLLOIDAL
AQUEOUS SOLUTIONS WITH RESONANT ULTRASOUND

Dissertation

zur

Erlangung des Doktorgrades (Dr. rer. nat.)

der

Mathematisch-Naturwissenschaftlichen Fakultät

der

Rheinischen Friedrich-Wilhelms-Universität Bonn

vorgelegt von

Nouri Mokhtar Elmiladi

aus

Tripolis, Libyen

Bonn 2010

Angefertigt mit Genehmigung der Mathematisch-Naturwissenschaftlichen Fakultät der Rheinischen Friedrich-Wilhelms-Universität Bonn.

1. Gutachter: Prof. Dr. Karl Maier
2. Gutachter: PD Dr. Reiner Vianden

Tag der Promotion: 21. Januar 2010

Erscheinungsjahr: 2010

Declaration

I hereby declare that the work in this thesis is original and has been carried out by me at the Helmholtz Institut für Strahlen- und Kernphysik, Universität Bonn, under the supervision of Prof. Dr. Karl Maier and in partial fulfillment of the requirements of the Doctor rerum naturalium (Dr. rer. Nat) degree of the University of Bonn. I further declare that this work has not been the basis for the awarding of any degree, diploma, fellowship, associateship of similar title of any university or institution.

Nouri Elmiladi

January 2010

Helmholtz Institut für Strahlen- und Kernphysik,

Universität Bonn,

Nußallee 14-16,

53115 – Bonn,

Germany

To
my dear blessed parents
and
my beloved wife and children

Abstract

Iron oxide nanoparticles have been extensively used in biomedical applications as a result of their magnetic properties. These magnetic nanoparticles are already used as contrast agents in magnetic resonance imaging (MRI). In this work, a method has been developed involving the application of ultrasound (US) while performing proton nuclear magnetic resonance spectroscopy to colloidal aqueous solutions. US is applied to samples of aqueous solutions containing specially prepared magnetic nanoparticles. The magnetic nanoparticles are chemically attached with antibody molecules from one side only such that their center of mass is different from their center of geometry. Two sizes of magnetic particles were used for measurements. $1.3 \mu\text{m}$ magnetic particles (MPs) were attached with IgM antibody molecules. 50 nm magnetic nanoparticles (MNPs) were attached with IgG antibody molecules. When subjected to US wave, these asymmetric particles tilted along with the vibrational movement. This behavior is effective on the change of the longitudinal relaxation rate only if the US frequency matches the proton Larmor frequency. To investigate this influence, an inversion recovery sequence was used. The amplitudes of the fast Fourier transform (FFT) of the free induction decays of the 90° read-out pulse were analyzed for different samples. No changes of the FFT amplitudes with and without US were observed for samples of distilled water and aqueous solutions of symmetric MNPs. However, a decrease in the FFT amplitudes with US turned on was observed for the aqueous solutions of asymmetric MNPs. The relative signal loss is greater for an aqueous solution containing 50 nm MNPs with IgG antibody molecules attached compared to an aqueous solution containing $1.3 \mu\text{m}$ MPs with IgM antibody molecules attached. This effect was observed particularly when the US frequency matched the proton Larmor frequency of the solvent. The measurements show that the relative signal loss with and without US depends on the power and pulse length of the applied resonant US.

Contents

1	Introduction	1
2	Theory	3
2.1	Nuclear Magnetic Resonance	3
2.1.1	Nuclear Spin System	3
2.1.2	Nuclear Magnetization	6
2.1.3	Relaxation	11
2.1.4	Pulse Sequences	18
2.2	MRI Contrast Agents	24
2.2.1	Magnetic Resonance Imaging	24
2.2.2	Contrast Agents	25
2.3	Ultrasound	27
2.3.1	Characteristics of Ultrasound	27
2.3.2	Production of Ultrasound Waves	28
3	Method	31
3.1	Principle	31
3.2	Sample Preparation	34
3.2.1	Experimental Setup for Sedimentation	35
3.2.2	Sedimentation Process	36
3.2.3	Final Preparation of Sample	38
4	Experimental Setup	39
4.1	NMR Electronics	39
4.1.1	The Magnet	39
4.1.2	Helmholtz Coils	39
4.1.3	Signal Processing Electronics	41
4.1.4	Sample Probe	42
4.2	Ultrasound Electronics	44
4.2.1	Ultrasound Emitter	44
4.2.2	Electromagnetic Crosstalk	45

5	Measurements and Results	47
5.1	Preliminary Measurement	47
5.2	Measurements of T_1	48
5.2.1	Method	48
5.2.2	Application of Ultrasound	49
5.3	Results	50
5.3.1	Water Sample	51
5.3.2	Sample of Aqueous Solution with $1.3 \mu\text{m}$ Magnetic Particles	52
5.3.3	Sample of Aqueous Solution with 50 nm Magnetic Nanoparticles . .	54
6	Discussion	57
7	Summary and Outlook	63
7.1	Summary	63
7.2	Outlook	64
A	Microscopic Pictures	65
B	Particles Technical Data	67
C	Graphs of FFT Amplitudes	69

Chapter 1

Introduction

Nuclear magnetic resonance (NMR) of protons in bulk matter was first demonstrated in 1946 independently by F. Bloch [1] and E. Purcell [2] who were jointly awarded the Nobel prize in 1952 for their discoveries. Their early demonstrations of proton NMR were soon followed by NMR investigation of other nuclei and by the use of NMR to characterize molecular and solid state environments. Today, NMR spectrometers are standard research tools in physics, chemistry, biology, geology, and perhaps most prominently, in medicine for magnetic resonance imaging (MRI) of human tissue.

Another subject of an increasing interest related to NMR is the interaction of acoustic waves with the nuclear spin system. This subject has been proposed since 1952 by Al'tshuler [3] and Kastler [4]. Al'tshuler predicted that the absorption of energy by a nuclear spin system from an externally generated acoustic wave should be observable. Thereafter, investigations were carried out, with the hope to display modifications of relaxation times within liquid and solid samples under the influence of ultrasound (US). There exist techniques for observing a nuclear spin resonance effect when coupling US with NMR in solids. Among these are acoustic saturation nuclear magnetic resonance (ASNMR) and nuclear acoustic resonance (NAR) [5].

In ASNMR both electromagnetic and acoustic energy is utilized and acoustic coupling to the nuclear spins is observed by its effect on the intensity of the nuclear magnetic resonance absorption. This effect was first observed indirectly in the acoustic saturation experiments of Proctor and Tantilla [6] on ^{35}Cl nuclei in NaClO_3 . Later, Menes and Bolef [7] have observed directly the absorption of acoustic energy at the resonance frequency and the double resonance frequency of ^{115}In nuclei in a single crystal of InSb .

In NAR, only acoustic energy is used for coupling to the nuclear spins. This coupling is observed as an absorption of energy from the source of US. NAR, like NMR, can be used as a spectroscopic tool. NMR uses electromagnetic radiation to induce energy level transitions, whereas NAR uses acoustic radiation. Polarized acoustic waves are generated and propagate within a specimen. If these perturbations are in resonance with the specimen's nuclear spin system, the acoustic waves will periodically modulate an internal magnetic dipole or electric quadrupole interaction as acoustic energy is absorbed. NAR has been observed in solids, and the first observation in metals was by Gregory and Bömmel [8] in 1965.

The effects of acoustic waves on the nuclear spins in liquids are less successful. In 1964 Bowen [9] reported that nuclear magnetic acoustic resonance saturation at the Larmor

frequency is negligibly small for non-viscous liquids owing to the effect of thermal motion. In 1966 he observed a proton acoustic nuclear magnetic resonance in certain liquids, but he confirmed that no effect is observed in a sample of distilled water [10]. Rotational motion, which has the dominating contribution to relaxation in water, is expected to be still less affected by acoustic waves [11, 12].

The idea of coupling US with magnetic resonance imaging to generate a better contrast has been investigated for some years by our group under the supervision of Prof. Maier. Early measurements in this area were carried out in 2005 [13]. In 2006 we observed initial results of an acoustic effect in a sample of distilled water using a spin echo sequence [14, 15, 16]. Applying an US pulse between the 90° and the 180° pulses causes the echo signal to diminish. This diminishing depends on the position, amplitude, and length of the US pulse. This effect was also observed even if the US frequency and the Larmor frequency were not in resonance.

Further measurements were conducted using aqueous solutions with suspended magnetic nanoparticles or piezoelectric nanoparticles to investigate the acoustic effect on the relaxation times of the solvent [17, 18]. Measurements using an inversion recovery sequence were carried out to examine the influence of resonant US on the spin-lattice relaxation time. Results obtained using the suspension of magnetic nanoparticles in the aqueous solutions were not affirmative. However, it was not clear whether this effect was acoustic or due to electromagnetic crosstalk. To distinguish between the two effects it has been proposed to use specially prepared magnetic nanoparticles instead of unmodified ones.

In this work, the influence of US on the spin-lattice relaxation rate of aqueous solutions with suspended specially prepared magnetic nanoparticles is experimentally examined. Because of the periodic US wave and in addition to the pressure fluctuations caused by the acoustic pressure, a motion is induced in liquids. This motion is an addition to the Brownian motion. It causes the modified magnetic nanoparticles to oscillate and tilt. Consequently, they generate a magnetic field in the near field. In resonance, the field couples to the protons of the solvent, and an increased spin-lattice relaxation is observed.

In Chapter 2, the theoretical basics of NMR and US are presented. Also, a description of MRI contrast agents is outlined.

In Chapter 3, the details regarding the experimental method and the techniques used to prepare the samples are described.

In Chapter 4, the experimental setup of the NMR and US electronics are explained.

In Chapter 5, the measurements and results obtained for different samples of aqueous solutions are presented.

Chapter 6 consists of a comparative discussion of the results obtained for different sizes of magnetic particles.

Finally, the conclusions drawn from the experimental work and suggestions of future applications are presented in Chapter 7.

Chapter 2

Theory

2.1 Nuclear Magnetic Resonance

NMR is a spectroscopic technique that relies on the magnetic properties of the atomic nucleus. When placed in a strong magnetic field, certain nuclei resonate at a characteristic frequency in the radio frequency range of the electromagnetic spectrum. Measuring the amount of energy absorbed by the nuclei at this resonant frequency gives us detailed information about the molecular structure in which the atom resides.

2.1.1 Nuclear Spin System

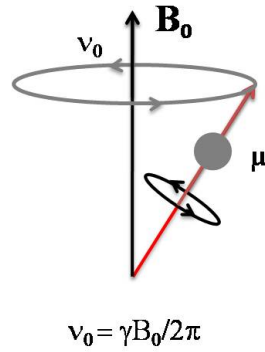
The nucleus of an atom consists of protons and neutrons and has a positive charge. It can be considered to rotate around an axis at a constant rate. This rotation is called spin. NMR is based on the interaction between nuclei that possess spin and an external magnetic field. Nuclear spin is one of several intrinsic characteristics of a nucleus and depends on the nuclear composition. Many nuclei are known to possess a non-zero spin angular momentum \mathbf{I} and a magnetic moment $\boldsymbol{\mu}$. These two vector quantities are parallel to each other and related by [19]

$$\boldsymbol{\mu} = \gamma\hbar\mathbf{I}, \quad (2.1)$$

where \hbar is the reduced Planck's constant, and γ is the gyromagnetic ratio which is a unique constant for each nuclear isotope possessing a spin. If a static magnetic field \mathbf{B}_0 is externally applied, the magnetic moments will experience a torque from the applied magnetic field which forces them to precess around the field direction with a characteristic frequency ν_0 , as shown in Figure 2.1.

The energy of interaction between the magnetic moment and the stationary field is defined by the following Hamiltonian [20]

$$\mathcal{H} = -\boldsymbol{\mu}\cdot\mathbf{B}_0 = -\gamma\hbar\mathbf{I}\cdot\mathbf{B}_0. \quad (2.2)$$



$$\nu_0 = \gamma B_0 / 2\pi$$

Figure 2.1: Precession of an isolated magnetic moment μ in a static magnetic field \mathbf{B}_0 . ν_0 is the characteristic frequency of precession.

Taking the field to be along the z-direction, i.e. $\mathbf{B}_0 = B_0 \hat{k}$, the eigenenergies of this Hamiltonian are

$$E_m = -m\gamma\hbar B_0 \quad m = I, I - 1, \dots, -I. \quad (2.3)$$

The number of allowed orientations is $2I + 1$ where I is the nuclear spin number. For example, hydrogen has only one proton as a nucleus which possesses spin $1/2$, i.e. $I = 1/2$. Then the two discrete spin states are $m = +1/2$ and $m = -1/2$. When placed in \mathbf{B}_0 , hydrogen nuclei (protons) either align themselves in the direction of the field or counter-align themselves in the field depending on which spin components they have ($+1/2$ or $-1/2$). Thus, the nuclei attain one of two energy states, a lower energy ($E_{+1/2} = -1/2\gamma\hbar B_0$) state for aligned nuclei and a higher energy ($E_{-1/2} = 1/2\gamma\hbar B_0$) state for counter-aligned nuclei. The difference between the two energy states is then

$$\Delta E = E_{-1/2} - E_{+1/2} = \gamma\hbar B_0. \quad (2.4)$$

This splitting of energy due to the presence of \mathbf{B}_0 is the nuclear Zeeman effect. It is represented in Figure 2.2.

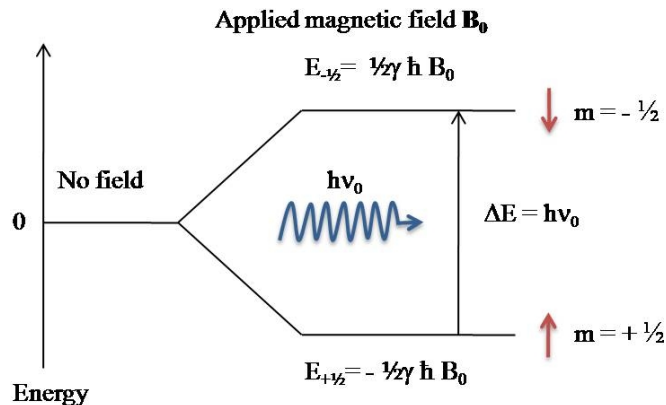


Figure 2.2: Zeeman energy levels diagram.

A nucleus in the lower energy state can be excited to the higher energy state by the absorption of a photon induced by an appropriate radio frequency (RF) field. The energy

of this photon ($h\nu_0$) must exactly match the energy difference (ΔE) between the two states [21].

$$h\nu_0 = \gamma\hbar B_0 \quad (2.5)$$

$$\nu_0 = \gamma B_0/2\pi \quad (2.6)$$

$$\omega_0 = 2\pi\nu_0 = \gamma B_0, \quad (2.7)$$

where h is Planck's constant, ω_0 is the angular velocity of the photon, and ν_0 is the photon frequency which is identical to the precession frequency of the magnetic moment about the applied magnetic field \mathbf{B}_0 . Equation (2.7) is called the Larmor relation, ω_0 is known as the Larmor velocity, and ν_0 is the Larmor frequency.

ν_0 is determined by the strength of \mathbf{B}_0 and the value of γ which is defined by

$$\gamma = \frac{e}{2m_p}g = g\mu_N/\hbar, \quad (2.8)$$

where e is the elementary charge, m_p is the proton rest mass, g is the g-factor, and $\mu_N = e\hbar/2m_p$ is the nuclear magneton. Equations (2.6) and (2.7) can be written as

$$\nu_0 = g\mu_N B_0/2\pi\hbar, \quad (2.9)$$

and

$$\omega_0 = g\mu_N B_0/\hbar. \quad (2.10)$$

For protons:

$$g_p = 5.58569, \quad \mu_N = 5.05078 \times 10^{-27} \text{ JT}^{-1}, \quad \gamma/2\pi = 42.577 \text{ MHz/T [22, 23]},$$

and

$$\nu_0 = 60.0 \text{ MHz for } B_0 = 1.41 \text{ T (Tesla)}.$$

Before applying the RF field, the spin system will in general be in thermal equilibrium with its surroundings called the lattice at a temperature T . The populations of the nuclear energy levels are then proportional to the Boltzmann factor [24]

$$N_m \propto \exp(-E_m/kT) = \exp(m\gamma\hbar B_0/kT), \quad \text{for protons,} \quad (2.11)$$

where k is the Boltzmann constant, and T is the absolute temperature of the spin system. For the case of protons where $m = -1/2, +1/2$, at equilibrium the lower energy level is more populated than the upper level and the population ratio of the two levels is

$$\frac{N_{-1/2}}{N_{+1/2}} = \exp(-\Delta E/kT) = \exp(-\gamma\hbar B_0/kT), \quad (2.12)$$

where $N_{-1/2}$ is the number of nuclei in the high energy level, and $N_{+1/2}$ is the number of nuclei in the low energy level. It is useful to define the nuclear polarization p as [25]

$$p = \frac{N_{+1/2} - N_{-1/2}}{N_{+1/2} + N_{-1/2}}, \quad (2.13)$$

where $p = 0$ means that there are equal numbers of protons in the two spin states and the sample is said to be unpolarized. For $p = +1$ or $p = -1$ all protons are in the spin up or spin down state, respectively. For 1.41 T magnetic field and samples kept at room temperature the polarization p is

$$p \approx 5 \times 10^{-6}, \quad (2.14)$$

which is an extremely small nuclear polarization. This means that of 400,000 protons in a sample at room temperature, about 200,001 are spin up and 199,999 are spin down. At room temperature the upper and lower energy spin states are almost equally populated with only a very small excess in the lower energy state. This nearly equal population distribution has a very important consequence. The signal intensity of any spectroscopic method depends largely on the population difference between the two energy levels involved. When a system is irradiated with a frequency, whose energy matches that separating the levels, transitions will be induced not only from the lower energy level to the higher, but also in the reverse direction. Upward transitions absorb energy while downward transitions release energy. The number of transitions in either direction is given by multiplying the starting level population by a probability. This probability is the same for transitions in either direction. If the energy level populations are the same, the number of transitions in either direction will also be the same. The absorption and release of energy will balance each other to zero and there will be nothing to observe. There is a net absorption or release of energy to observe only when the populations are not equal [26].

2.1.2 Nuclear Magnetization

The sum of the individual magnetic moments of all the protons contained in a macroscopic sample is referred to as the nuclear magnetization of the sample \mathbf{M} . The nuclear magnetization is defined as the net magnetic moment per unit volume. As a reminder in the following texts, the magnetization is always meant to be the nuclear magnetization. The magnitude of the net magnetization at thermal equilibrium, M_0 , of a sample containing N spins is given by [24]:

$$M_0 = \frac{N\gamma^2\hbar^2 I(I+1)}{3kT} B_0 = \chi_0 B_0, \quad (2.15)$$

where χ_0 is the static nuclear susceptibility. In a static field \mathbf{B}_0 the phases of an ensemble of precessing magnetic moments are at random, i.e. each magnetic moment has a random position in the precessional orbit induced by the static field. Due to this random phase

relationship, the transverse components of the individual spins cancel out. Since at equilibrium there is a small excess of nuclei in the lower energy state precessing about the axis of \mathbf{B}_0 , \mathbf{M} is pointing in the direction of \mathbf{B}_0 . This is illustrated in Figure 2.3.

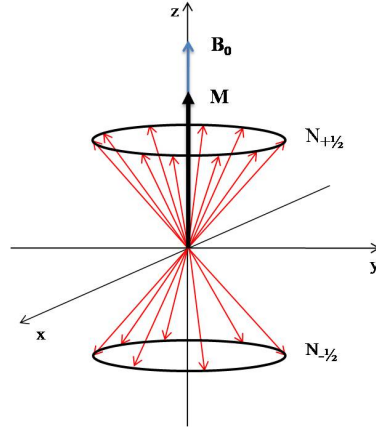


Figure 2.3: Spin 1/2 nuclei at equilibrium, prior to application of the \mathbf{B}_1 field.

Motion of a Magnetic Moment in a Static Magnetic Field

A magnetic moment \mathbf{M} in a uniform magnetic field \mathbf{B}_0 experiences a torque given by

$$\boldsymbol{\tau} = \mathbf{M} \times \mathbf{B}_0, \quad (2.16)$$

where

$$\boldsymbol{\tau} = \hbar \frac{d\mathbf{I}}{dt} = \frac{1}{\gamma} \frac{d\mathbf{M}}{dt}. \quad (2.17)$$

From equations (2.16) and (2.17), the motion of the magnetic moment is described classically as

$$\frac{d\mathbf{M}}{dt} = \gamma(\mathbf{M} \times \mathbf{B}_0). \quad (2.18)$$

Equation (2.18) shows that the vector describing the rate of change of \mathbf{M} is perpendicular to both \mathbf{B}_0 and \mathbf{M} . In order to solve this equation it is convenient to introduce a rotating coordinate system.

Let $S'(x',y',z')$ be a frame of reference rotating with respect to the laboratory frame $S(x,y,z)$ with an angular velocity represented by the vector $\boldsymbol{\omega}$. According to the general law of relative motion, the time derivative $d\mathbf{A}/dt$ of any time dependent vector $\mathbf{A}(t)$ computed in the laboratory frame S , and its derivative $\delta\mathbf{A}/\delta t$ computed in the rotating frame S' are related through [27]

$$\frac{d\mathbf{A}}{dt} = \frac{\delta\mathbf{A}}{\delta t} + \boldsymbol{\omega} \times \mathbf{A}, \quad (2.19)$$

or

$$\frac{\delta \mathbf{A}}{\delta t} = \frac{d\mathbf{A}}{dt} - \boldsymbol{\omega} \times \mathbf{A}. \quad (2.20)$$

Similarly, the equation of motion of \mathbf{M} can be written in terms of a coordinate system rotating at $\boldsymbol{\omega}$ as

$$\frac{\delta \mathbf{M}}{\delta t} = \frac{d\mathbf{M}}{dt} - \boldsymbol{\omega} \times \mathbf{M} = \gamma(\mathbf{M} \times \mathbf{B}_0) + \mathbf{M} \times \boldsymbol{\omega} \quad (2.21)$$

$$\frac{\delta \mathbf{M}}{\delta t} = \gamma \mathbf{M} \times \mathbf{B}_e, \quad (2.22)$$

where \mathbf{B}_e is the effective field in the rotating frame and is given by

$$\mathbf{B}_e = \mathbf{B}_0 + \frac{\boldsymbol{\omega}}{\gamma}, \quad (2.23)$$

with $\mathbf{B}_0 = B_0 \hat{k}$. If the rotating frame has an angular velocity $\boldsymbol{\omega}$ such that $\boldsymbol{\omega} = -\gamma \mathbf{B}_0 = -\gamma B_0 \hat{k}$, the effective field in the rotating frame vanishes, and

$$\frac{\delta \mathbf{M}}{\delta t} = 0. \quad (2.24)$$

Therefore, \mathbf{M} is a fixed vector in the rotating frame. This means that in the laboratory frame, \mathbf{M} precesses about \mathbf{B}_0 at ω_0 . When a frame of reference is rotating at the Larmor frequency, the magnetic field (which gave rise to the precession at the Larmor frequency) is zero in the rotating frame and

$$\boldsymbol{\omega}_0 = -\gamma \mathbf{B}_0. \quad (2.25)$$

Motion of a Magnetic Moment in a Rotating Magnetic Field

Suppose that a second magnetic field ($\mathbf{B}_1 = B_1 \hat{i}$) is applied along the x -axis in the rotating frame S' perpendicular to \mathbf{B}_0 . \mathbf{B}_1 is rotating around \mathbf{B}_0 with an angular velocity $\boldsymbol{\omega}$. The Bloch equation describing the motion of the magnetic moment in the presence of both \mathbf{B}_0 and \mathbf{B}_1 fields can then be written as

$$\frac{d\mathbf{M}}{dt} = \gamma \mathbf{M} \times (\mathbf{B}_0 + \mathbf{B}_1). \quad (2.26)$$

The equation of motion of \mathbf{M} can be written in terms of a coordinate system rotating at $\boldsymbol{\omega}$ as

$$\frac{\delta \mathbf{M}}{\delta t} = \frac{d\mathbf{M}}{dt} - \boldsymbol{\omega} \times \mathbf{M} = \gamma \mathbf{M} \times (\mathbf{B}_0 + \mathbf{B}_1) + \mathbf{M} \times \boldsymbol{\omega}, \quad (2.27)$$

which can be shortened to

$$\frac{\delta \mathbf{M}}{\delta t} = \gamma \mathbf{M} \times \mathbf{B}_e. \quad (2.28)$$

The total effective field \mathbf{B}_e , which is shown in Figure 2.4, is static in S' and is given by

$$\mathbf{B}_e = \mathbf{B}_0 + \mathbf{B}_1 + \frac{\boldsymbol{\omega}}{\gamma}, \quad (2.29)$$

where $\mathbf{B}_0 = B_0 \hat{k}$, $\mathbf{B}_1 = B_1 \hat{i}$, and $\boldsymbol{\omega} = -\omega \hat{k}$.

$$\mathbf{B}_e = \left(B_0 - \frac{\omega}{\gamma}\right) \hat{k} + B_1 \hat{i}. \quad (2.30)$$

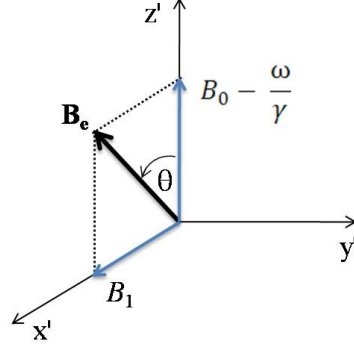


Figure 2.4: Effective magnetic field \mathbf{B}_e in the rotating frame of reference.

The magnitude of \mathbf{B}_e is

$$B_e = \left[\left(B_0 - \frac{\omega}{\gamma} \right)^2 + B_1^2 \right]^{\frac{1}{2}} = \frac{a}{\gamma}, \quad (2.31)$$

and the angle (θ) between \mathbf{B}_e and \mathbf{B}_0 is given by

$$\tan \theta = \frac{B_1}{B_0 - \frac{\omega}{\gamma}} = \frac{\omega_1}{\omega_0 - \omega}, \quad (2.32)$$

$$\sin \theta = \frac{\omega_1}{a} \quad \cos \theta = \frac{\omega_0 - \omega_1}{a}$$

where ω is the rate of precession of \mathbf{B}_1 about \mathbf{B}_0 , $\omega_1 = \gamma B_1$, $\omega_0 = \gamma B_0$, and

$$a = - \left[(\omega_0 - \omega)^2 + \omega_1^2 \right]^{\frac{1}{2}} \frac{\gamma}{|\gamma|}. \quad (2.33)$$

From equation (2.32) θ is never large or the effect of \mathbf{B}_1 is negligible unless $\omega \approx \omega_0$ or $\omega_0 - \omega \approx \omega_1$. The width of the resonance, that is, the value of the difference $(\omega_0 - \omega)$ below which the effect is appreciable is of the order of ω_1 . If a linearly polarized field is composed of two components, one rotating with angular frequency of ω , then the other has an angular frequency of $(-\omega)$. At resonance, for one component $\omega = \omega_0$ and for the second $\omega = -\omega_0$. For the second component

$$\tan \theta = \frac{\omega_1}{2\omega_0}, \quad (2.34)$$

and hence $\theta \approx 0$ because $\omega_1 \ll \omega_0$. Thus, absorption of power is due only to the component where $\omega = \omega_0$.

At equilibrium the net magnetic moment is aligned with \mathbf{B}_0 which is taken to be the z -direction. The resulting magnetization is called longitudinal magnetization, M_z . Thus, at $t = 0$, \mathbf{M} is defined as

$$\mathbf{M}(t = 0) = M_z \hat{k} \quad (2.35)$$

$$M_z(0) = M_0, \quad (2.36)$$

and $M_0 = \chi_0 B_0$ is the thermal equilibrium magnetization. If a rotating magnetic field \mathbf{B}_1 is applied for a finite period of time in the form of radio frequency (RF) pulse, the magnetization vector \mathbf{M} will be moved away from its equilibrium state. \mathbf{M} will be tipped away from the z -axis towards the xy -plane at an angle α (in radians). This angle is often referred to as the “flip angle” and is dependent on the shape of the pulse and its duration. This angle is given by

$$\alpha = \gamma B_1 t, \quad (2.37)$$

where B_1 is the amplitude of the RF signal, and t is the time over which the oscillating field is applied. Increasing the B_1 amplitude or increasing the time over which the field is applied will increase the flip angle. For example, setting $\alpha = \gamma B_1 t = \pi/2$ results in a 90° pulse which will nutate the net magnetization from the longitudinal plane to the transverse plane as shown in Figure 2.5. The protons continue to precess along the \mathbf{B}_1 axis while revolving around the \mathbf{B}_0 axis. For effective tipping, the frequency of \mathbf{B}_1 should be equal to the Larmor frequency.

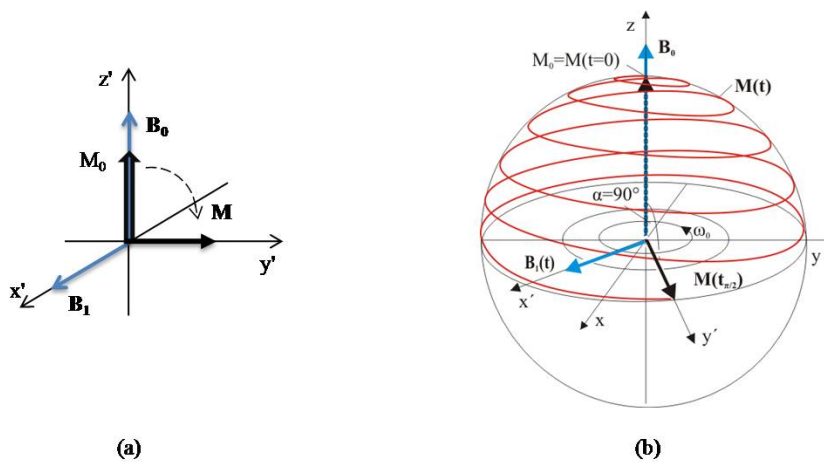


Figure 2.5: Nutation of the precessing net magnetization \mathbf{M} as a function of time caused by application of a radio frequency 90° pulse. Motion is shown (a) in the rotating frame of reference (b) in the laboratory frame of reference.

Similarly, a pulse of the same amplitude but twice as long will simply invert the longitudinal magnetization to point along the negative z -axis. This results in a 180° pulse or π pulse. The application of a combination of 90° and 180° pulses can be used to create an NMR pulse sequence.

When the spin system is excited, it initially behaves coherent which means that the magnetization of all the components in the system are in phase. There is also a component of \mathbf{M} present in the xy -plane called the transverse magnetization M_{xy} that precesses about the z -axis. As soon as the RF signal is turned off, the precessing transverse magnetization starts to decay due to proton relaxation processes, as discussed further below. The transverse magnetization must return to zero and the longitudinal magnetization must return to its equilibrium value.

2.1.3 Relaxation

After the net equilibrium magnetization \mathbf{M} has been disturbed by \mathbf{B}_1 irradiation at the Larmor frequency, the system relaxes. That is, the populations return to their former Boltzmann distribution by giving up their excess energy to the surrounding environment or lattice. This transfer of energy to the lattice is known as the longitudinal or spin-lattice relaxation and is characterized by a time constant T_1 called the spin-lattice relaxation time. A second type of relaxation occurs in the spin system that does not involve an exchange of energy with the lattice, but rather a loss of spin coherence. This process is called the transverse or spin-spin relaxation with a characteristic time denoted by T_2 . Measurements of T_1 and T_2 lead to information about molecular structure and mobility. Longitudinal relaxation corresponds to longitudinal magnetization M_z recovery, and transverse relaxation corresponds to transverse magnetization M_{xy} decay. The time rate of change of M_z and M_{xy} magnetizations [1] are given by

$$\frac{dM_z}{dt} = -\frac{(M_z - M_0)}{T_1}, \quad (2.38)$$

and

$$\frac{dM_{xy}}{dt} = -\frac{M_{xy}}{T_2}. \quad (2.39)$$

T_1 relaxation is a process by which the longitudinal magnetization M_z attains its equilibrium value M_0 . If at any time the longitudinal magnetization is not equal to M_0 , it will exponentially approach the equilibrium value. On the other hand, T_2 relaxation is a process by which the transverse M_{xy} vanishes. If at any time the transverse magnetization is not equal to zero, it will exponentially decay to zero. Thus, if at time $t = 0$ the longitudinal magnetization is $M_z(0)$ and the transverse magnetization is $M_{xy}(0)$, the components of the magnetization at time t will be:

$$M_z(t) = M_z(0) \exp(-t/T_1) + M_0[1 - \exp(-t/T_1)], \quad (2.40)$$

and

$$M_{xy}(t) = M_{xy}(0) \exp(-t/T_2). \quad (2.41)$$

Spin-Lattice Relaxation

The return to equilibrium of the spin system via the spin-lattice relaxation process involves the transitions of protons from the higher energy level (spin down) to the lower energy level (spin up). The recovery rate of the longitudinal magnetization M_z is characterized by T_1 , and the inverse of the longitudinal relaxation time $1/T_1$ is referred to as the longitudinal relaxation rate R_1 . This process corresponds to the total magnetic moment realigning over time with the static \mathbf{B}_0 , i.e. the restitution of the z -component of magnetization.

For example, following a 90° excitation pulse, the nuclear magnetization precesses in the xy -plane about the z -axis, i.e. $M_z(0) = 0$. The growth of the longitudinal magnetization in the z -axis is then described by the following exponential relation:

$$M_z(t) = M_0[1 - \exp(-t/T_1)]. \quad (2.42)$$

This is shown in Figure 2.6 where M_z grows from zero to M_0 . After time T_1 , M_z will have recovered to within a factor $[1 - (1/e)] = 63\%$ of the equilibrium value M_0 .

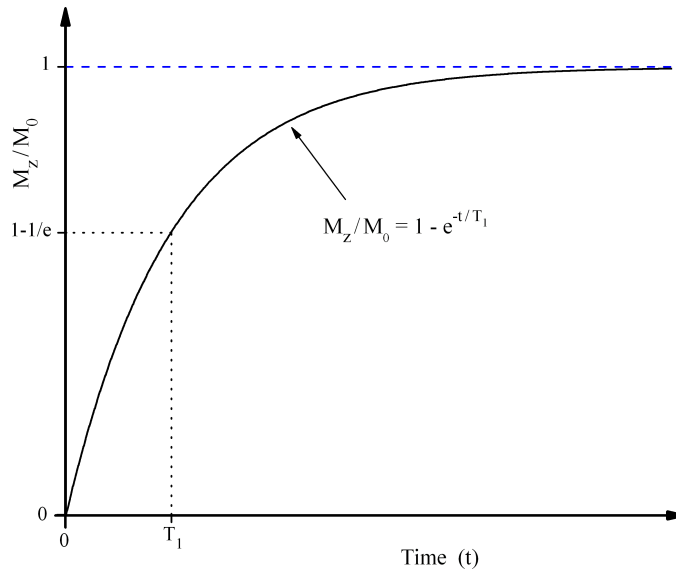


Figure 2.6: T_1 relaxation curve shows the recovery of longitudinal magnetization $M_z(t)$ after a 90° pulse.

There are several ways to measure T_1 , but the two most common double pulse sequence techniques are the saturation recovery method [28] and the inversion recovery sequence [29]. The latter will be discussed in more details in section 2.1.4.

Excited protons can go from their high energy state to the low energy state while emitting photons through spontaneous emission or stimulated emission. However, at radio frequencies spontaneous emission is insignificant because its probability varies with the cube of the frequency. Spin-lattice relaxation occurs because of the existence of magnetic fields fluctuating at the Larmor frequency in the xy -plane which are able to induce these transitions. The excited spins interact with these local fields and transfer energy to the lattice as thermal energy [26].

T_1 is dependent on local fields caused by molecular movement that can be described by a correlation time τ_c which is the average time required for a molecule to rotate one

radian [30]. Small molecules tumble rapidly and have a short τ_c , whereas large molecules tumble slowly and have a longer τ_c . The correlation time varies due to molecular size, solvent viscosity and temperature. Relaxation is most efficient when the tumbling rate ($1/\tau_c$) and the resonance frequency (ω_0) in *radians/s* are comparable in magnitude, i.e. $\omega_0\tau_c \approx 1$. The most common source of the fluctuating field is tumbling of a nearby magnetic dipole. Tumbling of a very small molecule can occur at a rate ω as high as 10^{12}s^{-1} . However, not all molecules in a given sample are tumbling at the same rate. The existence of a range of tumbling rates within a sample means that there is also a range of magnetic fields that they generate. The concentration of fields at a particular frequency is called the spectral density $J(\omega)$. The value of the spectral density at the resonance frequency $J(\omega_0)$ is critical for relaxation to be efficient. In the case of small molecules that tumble at rates around 10^{12}s^{-1} , their spectral density at a desirable range of ω_0 , $10^8 - 10^9$ radian/s, is low ($1/\tau_c \gg \omega_0$). This situation is illustrated in Figure 2.7a. Relaxation rates increase with larger molecules, as the tumbling rate slows ($\omega_0\tau_c \approx 1$), as in Figure 2.7b. The spectral density now is sufficiently high at the Larmor frequency to provide efficient relaxation. For very large, slowly tumbling molecules, the plot, as in Figure 2.7c, backs off further and has a very low value at the Larmor frequency ($1/\tau_c \ll \omega_0$).

The relation between the spectral density function and the correlation time in terms of the tumbling frequency is expressed as [30]:

$$J(\omega) = G(0) \frac{2\tau_c}{(1 + \omega^2\tau_c^2)}, \quad (2.43)$$

where $G(0)$ is the variance or the mean-square amplitude of the interaction leading to relaxation. The long, flat portion of the plot of $J(\omega)$ against ω for different correlation times in Figure 2.7 corresponds to the region in which $1/\tau_c$ is much greater than ω , so that $\omega^2\tau_c^2 \ll 1$ and $J(\omega) \propto 2\tau_c$ (a constant). In this region the relaxation rate is independent of the Larmor frequency, and it is called the extreme narrowing region.

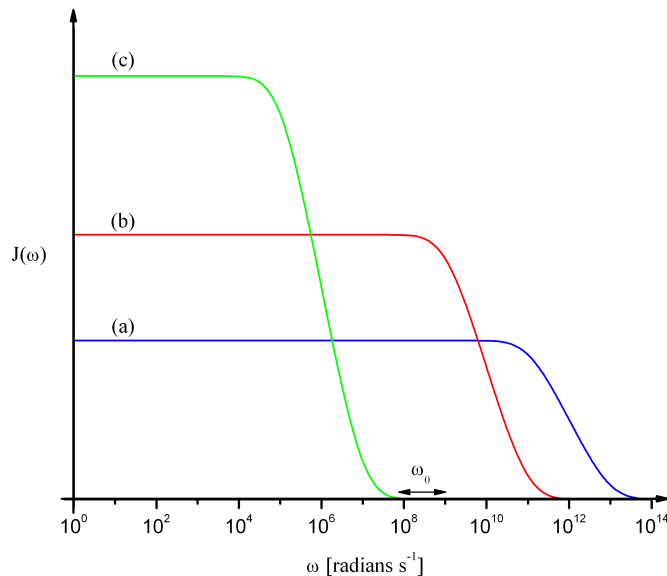


Figure 2.7: Plot of spectral density vs. logarithm of tumbling frequency. The three curves must enclose the same area (in the linear scale), but their upper limits vary.

The spin-lattice relaxation rate, $R_1 = T_1^{-1}$, is directly related to the spectral density function at the Larmor precession frequency of the nucleus ($T_1^{-1} \sim J(\omega_0)$). An expression for T_1^{-1} with respect to τ_c is written as:

$$T_1^{-1} \propto \frac{2\tau_c}{(1 + \omega_0^2\tau_c^2)}. \quad (2.44)$$

Since relaxation is most efficient when $\omega_0\tau_c \approx 1$, T_1 goes through a minimum (R_1 achieves its maximum) when plotted against the correlation time. Thus, the T_1 minimum is dependent on the resonance frequency. It occurs as the spectral density moves off the long, flat region and quickly drops to zero. Figure 2.8 shows T_1 as calculated by Bloembergen, Purcell, and Pound [31] as a function of the correlation time τ_c .

Under the extreme narrowing condition where $\omega_0^2\tau_c^2 \ll 1$, $T_1^{-1} \propto 2\tau_c$. Thus, T_1 decreases as τ_c increases. This regime is depicted for T_1 at the left of Figure 2.8; note that T_1 is independent of the resonance frequency ω_0 here. When $1/\tau_c$ is even shorter, $\omega_0^2\tau_c^2 \gg 1$, and $T_1^{-1} \propto 2/(\omega_0^2\tau_c)$. In this regime, T_1 and τ_c are directly proportional. Thus, T_1 increases as τ_c increases, i.e. as the mobility decreases.

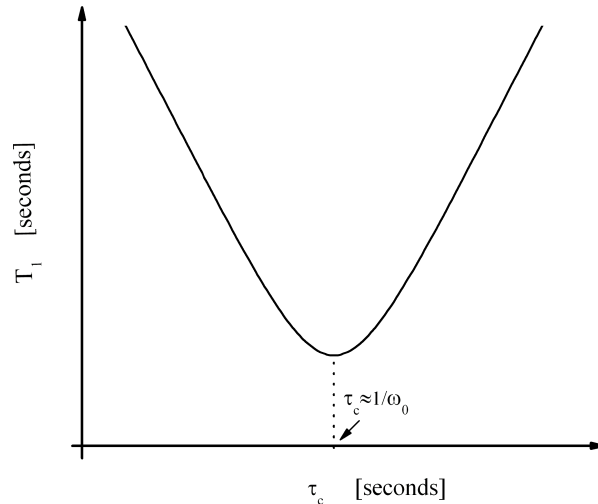


Figure 2.8: Relationship between T_1 and τ_c . The region to the left of T_1 minimum is that of very rapid molecular motion. The region to the right of T_1 minimum is the rigid lattice regime.

Spin-lattice relaxation can occur by several mechanisms by which spins can be induced to drop down and reestablish the Boltzmann equilibrium. Some of these mechanisms are presented here each of which contributes to the spin-lattice relaxation process with its own relaxation rate R_1 :

Nuclear Dipole-Dipole Relaxation (R_1^{DD}): A magnetic nucleus in motion generates an instantaneous magnetic dipolar field whose frequency depends on the rate of motion and on the magnetic moment of the dipole. The resulting magnetic field can fluctuate at the same frequency as the resonance frequency of the nucleus in question, permitting energy to transfer from excited spins to the lattice. Such a process is called dipole-dipole relaxation because it involves interaction of the resonating nuclear magnetic dipole with the dipole of the nucleus in motion that causes the fluctuating field of the lattice. This fluctuating field constitutes a mechanism for

relaxation of nearby spins. The resulting relaxation rate depends on the nuclear moments of the interacting nuclei and on the distance between them. As a result, nuclear spin relaxation can be used to determine distances between nuclei. Protons have a large gyromagnetic ratio; therefore, dipole-dipole interactions cause the most efficient relaxation of proton spins and constitute a sensitive probe for internuclear distances.

Chemical Shift Anisotropy Relaxation (R_1^{CSA}): A proton in a chemical compound finds itself bound within a molecule which in most cases is slightly shielded from the external magnetic field B_0 by the surrounding electron cloud. This shielding varies with the nature of the chemical group containing the nucleus. If the magnetic field is homogeneous, separate NMR frequency peaks are obtained at different positions. The resulting shift of the NMR frequency is called a chemical shift [32]. The chemical shift (δ) of a nucleus is expressed in parts per million (ppm), and is defined as the difference between the resonance frequency of the nucleus ν_{sample} and a reference ν_0 , relative to the reference frequency:

$$\delta = \frac{\nu_{sample} - \nu_0}{\nu_0} \times 10^6 \text{ ppm}. \quad (2.45)$$

Because shielding at the nucleus varies with the orientation of the molecule with respect to the B_0 field (chemical shift anisotropy), the magnetic field acting on the nucleus varies (except for extremely symmetrical molecules). Therefore, molecular tumbling modulates the local field and provides a mechanism for relaxation. This mechanism becomes more important at higher fields.

Paramagnetic Relaxation (R_1^{Para}): The electron has a magnetic moment μ_e more than three orders of magnitude greater than the nuclear magnetic moment of the proton μ_p . Consequently, dipolar interactions between a nucleus and an unpaired electron in a tumbling molecule are extremely strong. The resulting fluctuating magnetic fields are quite effective at producing relaxation. Thus, paramagnetic impurities can shorten the relaxation time T_1 [33]. Relaxation agents containing unpaired electrons, such as paramagnetic metal ions, are sometimes introduced intentionally at trace levels in order to shorten relaxation times [34]. Paramagnetic compounds are widely used as contrast agents for magnetic resonance imaging, as discussed later in section 2.2.2.

Relaxation with Ferromagnetic Particles (R_1^{Ferro}): Ferromagnetic nanoparticles have large magnetic moments, thus they are more sensitive than paramagnetic compounds. Suspension of magnetite (Fe_3O_4) particles in aqueous solutions leads to reductions in T_1 and T_2 relaxation times of surrounding water protons [35]. Iron oxide nanoparticles are also commonly used as contrast agents for magnetic resonance imaging, as discussed later in section 2.2.2.

Quadrupolar Relaxation (R_1^{Quad}): If a nucleus has a spin $I > 1/2$, it is characterized by a non-spherical distribution of electrical charges and possesses an electric quadrupole moment. The interaction of the quadrupole moment with local oscillating electric field gradients (due to electrons) provides a relaxation mechanism [36]. Quadrupolar interactions can be very large and efficient for promoting relaxation. Quadrupolar nuclei display broad resonance lines in NMR spectra, unless the nuclei are in highly

symmetric electronic environment (which reduces the magnitudes of the electric field gradients at the locations of the nuclei).

Cross Relaxation (R_1^{Cross}): In large molecules and solids there is insufficiently rapid tumbling to average out all the intramolecular interactions, and energy is efficiently exchanged between nuclear spins. If water molecules are bound to macromolecules, then relaxation processes in the large molecule are transferred to the bound water by cross relaxation [37, 38]. This interaction can be exploited in magnetic resonance imaging because it can generate useful contrast.

Scalar Coupling Relaxation (R_1^{SC}): The effect of scalar coupling relaxation on T_1 is more significant when the two interacting nuclei have very close Larmor frequencies such as ^{13}C and ^{79}Br [39]. Scalar relaxation is more important for the T_2 relaxation as with this mechanism the quadrupolar nuclei can broaden lines significantly on nuclei that are coupled to it.

Spin Rotation Relaxation (R_1^{SR}): Coherent intramolecular rotations generate a magnetic field. These rotations are interrupted by molecular collisions, causing the magnetic field to change. Relaxation by spin rotation is faster at higher temperature, and this mechanism is very important for very small molecules [40].

When multiple mechanisms contribute to relaxation, the total effective relaxation rate would be the sum of all contributions; that is,

$$R_1 = R_1^{DD} + R_1^{CSA} + R_1^{Para} + R_1^{Ferro} + R_1^{Quad} + R_1^{Cross} + R_1^{SC} + R_1^{SR} + R_1^X, \quad (2.46)$$

where R_1^X is the relaxation rate of any other possible spin-lattice relaxation mechanism that was not mentioned here. The DD interaction is a dominant contribution to T_1 relaxation and causes the most efficient relaxation of protons in molecules in solution.

Spin-Spin Relaxation

Directly after an excitation pulse, all the protons precess in phase and their individual magnetic moments will collectively contribute to the transverse magnetization. The transverse or spin-spin relaxation is a process in which the transverse magnetization M_{xy} decays following the excitation pulse. This decay is characterized by the time constant T_2 . For the specific case of a 90° pulse, immediately after its application, the net magnetization vector is in the xy -plane, i.e. $M_{xy}(0) = M_0$. Hence, the decay of the transverse magnetization is described by the following exponential relationship:

$$M_{xy}(t) = M_0 \exp(-t/T_2). \quad (2.47)$$

T_2 relaxation can be described as a curve in Figure 2.9. After time T_2 , transverse magnetization will have lost 36% of its original value. To measure T_2 , a spin-echo sequence is used which will be explained in section 2.1.4.

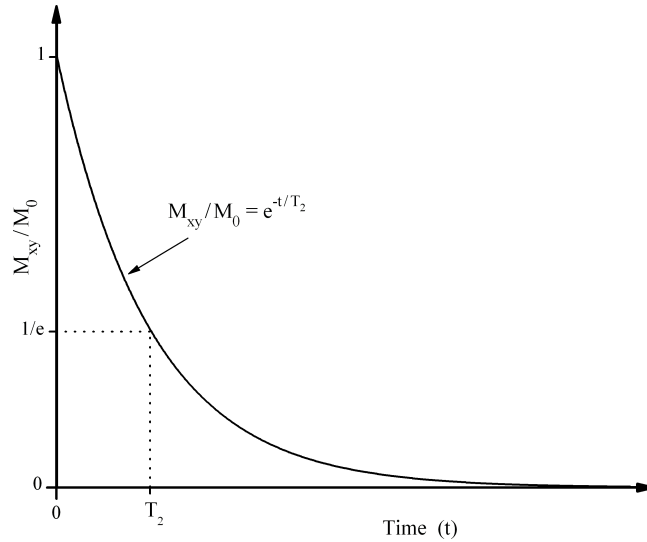


Figure 2.9: T_2 relaxation curve shows the decay of transverse magnetization after a 90° pulse.

If T_2 relaxation were slower than T_1 relaxation, then the transverse magnetization would have not dephased by the time the sample had returned to equilibrium. This is physically impossible, as once the sample has returned to equilibrium, there is no magnetization perpendicular to the original direction. Hence, $T_1 \geq T_2$. In any medium (except pure water) the decay of M_{xy} occurs significantly faster than the recovery of M_z due to additional relaxation effects affecting the net magnetization in the transverse plane. The relaxation in the xy -plane is driven by the loss of phase coherence in the precessing protons due to:

Spin-Spin Interactions: This mechanism involves the interaction of two nuclei with opposite spin. The process whereby one spin goes from $+1/2$ to $-1/2$ while the other goes from $-1/2$ to $+1/2$ involves no net change in the longitudinal magnetization and hence no spin-lattice relaxation. The switch in spins results in dephasing because the new spin state has a different phase from the old one. As this process continues, the phases become randomized around the z -axis, and the transverse magnetization disappears. This process of two nuclei simultaneously exchanging spins is sometimes called the flip-flop mechanism.

Magnetic Field Inhomogeneity: A similar result arises when the static field \mathbf{B}_0 is not perfectly homogeneous. If there are inhomogeneities in the static magnetic field over the dimensions of the sample then different magnetic moments will precess at different rates. In other words, some components of the magnetization start getting ahead of the average and some start getting behind. As the spins precess faster or more slowly relative to each other, eventually their relative phases become equally distributed. This results in a shortening of the transverse relaxation time. The time constant which describes the decay of the magnetization in the xy -plane when magnetic inhomogeneities are included is designated T_2^* . The exponential shape of the free induction tail depends on T_2^* which is always smaller than T_2 . In the limit of very homogeneous fields, T_2^* approaches T_2 . The relationship between T_2^* and T_2 is:

$$\frac{1}{T_2^*} = \frac{1}{T_2} + \frac{1}{T_{inhom.}} = \frac{1}{T_2} + \gamma \frac{\Delta B_0}{2}, \quad (2.48)$$

γ represents the gyromagnetic ratio, and ΔB_0 is the variation in the field brought about either through distortions in the homogeneity of the applied field itself, or by local variations in the magnetic susceptibility of the system [41, 42].

2.1.4 Pulse Sequences

In order to detect a signal, resonance needs to be established [43]. The term resonance implies alternating absorption and dissipation of RF energy. Therefore, to measure the resonant frequency, nuclei must absorb or emit RF energy. If the sample, nuclei in an NMR experiment are in a sample, is subjected to an oscillating magnetic field provided by a coil, a spin in the lower energy state can be “bumped” into the higher energy state if the radio frequency is exactly equal to the Larmor frequency, ν_0 .

An ^1H NMR spectrometer is designed to detect the NMR signal of protons and to record a frequency spectrum. The actual procedure for obtaining the spectrum varies. One of the earliest and simplest applications of NMR spectroscopy is the continuous wave or CW NMR [2]. In this kind of spectroscopy, both the magnetic field \mathbf{B}_0 and the RF excitation signal are continuously on. Either the magnetic field \mathbf{B}_0 is kept constant and the frequency of the rotating magnetic field \mathbf{B}_1 varied, or \mathbf{B}_0 is varied while keeping the input frequency constant. Either approach allows sweeping through the resonance of the sample under investigation.

Modern NMR spectrometers, including the one used here, operate in the “pulsed Fourier-transform” (FT) mode [1], permitting the entire spectrum to be recorded in two to three seconds rather than the slow (5 min) frequency sweep. The rotating magnetic field \mathbf{B}_1 is provided in the form of a short RF pulse which excites all of the protons in the sample. \mathbf{B}_1 is a sinusoidal varying field in a fixed direction. It is obtained by inducing an electrical voltage in a coil, placed around the sample, whose axis is perpendicular to the direction of the static field \mathbf{B}_0 . Immediately after the pulse is over, the nuclei are organized in such a way that their precessing magnetic moments sum together to form a net magnetization of the sample, which rotates at ν_0 . The coil that is used to transmit RF energy is also used as a receiver. A signal, which oscillates in time at ν_0 , is observed and recorded. Then, the fast Fourier transform (FFT) converts the signal to a spectrum, a graph of intensity versus frequency.

NMR spectroscopy requires the application of RF pulses to the sample to obtain coherent signals from the receiving coil. These pulses are applied in specific sequences to produce NMR signals that yield information about the sample. All pulse sequences have in common the use of RF pulses to nutate the bulk magnetization vector at some angle with respect to the static magnetic field.

Free Induction Decay

During, and immediately after the application of an excitation pulse (except in the case of a perfect 180° pulse), there will be a component of \mathbf{M} present in the xy -plane (M_{xy}) that rotates about the z -axis. The rotating nature of M_{xy} makes it possible to detect the presence of this magnetization component through an induction of a current in the receiver coil. The maximum signal is obtained when the net equilibrium magnetization is nutated 90° to precess in the xy -plane at the resonance frequency. Such a pulse has

the effect of establishing phase coherence in the sample. Immediately after the 90° pulse, the proton population begins to lose coherence and as a result the induced signal decays exponentially to zero. This decay of the signal is called the free induction decay (FID) as shown in Figure 2.10a. The initial amplitude of the signal is determined by the portion of the magnetization vector (M_0) that has been tipped onto the xy -plane. The FID is a time dependent voltage response signal which decays with the time constant T_2^* at the rate $\exp(-t/T_2^*)$.

Since the FID is in the time domain, and data in the frequency domain is required, a Fourier transform of the data becomes necessary. Converting between the frequency domain and the time domain requires the following two equations [44],

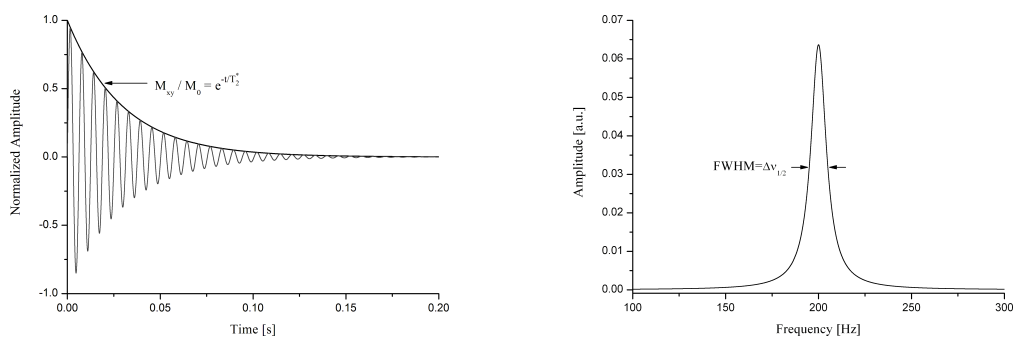
$$F(\omega) = \int_{-\infty}^{+\infty} f(t)e^{-i\omega t} dt \quad (2.49)$$

$$F(t) = \int_{-\infty}^{+\infty} f(\omega)e^{i\omega t} dk. \quad (2.50)$$

where t is the time, ω is the frequency. f is a function in either the time or frequency domain, and F is the same function converted into the Fourier conjugate domain. By applying these equations to an FID all of the frequencies present can be determined. If there is only one frequency present, then the FFT of the FID gives a frequency domain spectrum, a Lorentzian line shape, with a single peak at the Larmor frequency as shown in Figure 2.10b. T_2^* is related to the linewidth in the frequency spectrum as:

$$\text{linewidth} = \Delta\nu_{1/2} = \frac{2}{T_2^*}, \quad (2.51)$$

where $\Delta\nu_{1/2}$ is the full width at half maximum (FWHM) of the frequency line.



(a) After application of a 90° pulse, the proton population dephases, and a free induction decay (FID) signal can be detected.

(b) Fast Fourier transformation (FFT) of the FID yields a frequency domain spectrum.

Figure 2.10: NMR spectrum.

When this sequence is repeated to obtain a better signal-to-noise ratio, the amplitude of the signal after being Fourier transformed will depend on T_1 and the time between

repetitions, called the repetition time (TR), of the sequence. If the RF is pulsed multiple times, the signal could be attenuated due to saturation of longitudinal polarization. The polarization will not fully build up before it is tipped again if the repetition time $TR < T_1$. In the limit $TR \rightarrow 0$, the signal will disappear because polarization will never rebuild. Often $TR > 5T_1$ is used as a rule of thumb for complete return to equilibrium.

Inversion Recovery Sequence

The inversion recovery method is a simple two-pulse sequence and is a convenient way to measure T_1 . In this sequence a 180° pulse inverts the spin population and thus the magnetization of the sample nuclei. If the original value of the magnetization was M_0 , its value immediately after the 180° pulse is $-M_0$. The magnetization undergoes spin-lattice relaxation and recovers to its original value. In other words, the magnetization vector, initially aligned with the negative z -axis, will gradually shrink back toward the xy -plane, pass through this plane and eventually make a full recovery along the positive z -axis with the characteristic time constant T_1 . Since magnetization along the z -axis is unobservable, the recovery is monitored by placing the vector back in the xy -plane with a 90° pulse after a suitable period τ following the initial inversion as shown in Figure 2.11. The delay between the 180° RF inversion pulse and the 90° RF excitation pulse is referred to as the inversion time (TI).

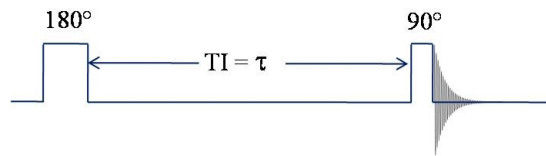


Figure 2.11: Inversion recovery sequence: a 90° pulse is applied at a delay time τ after the application of a 180° pulse.

Once magnetization is present in the xy -plane, it rotates about the z -axis and dephases giving an FID signal. The magnitude of the FID signal and the amplitude of the FFT of the FID (the peak height of the spectrum) should be directly proportional to the longitudinal magnetization of the sample just before the 90° pulse. If τ is zero, the magnetization vector terminates with full intensity along the negative y -axis producing an inverted spectrum using conventional spectrum phasing, that is, defining the positive y -axis to represent positive absorption. Repeating the experiment with increasing values of τ allows one to follow the relaxation of the spins in question as illustrated in Figure 2.12. Finally, when τ is sufficiently long ($\tau_\infty > 5T_1$), complete relaxation will occur between the two pulses and the maximum positive signal is recorded. The intensity of the detected magnetization $M_z(\tau)$ follows:

$$M_z(\tau) = M_0(1 - 2\exp(-\tau/T_1)), \quad (2.52)$$

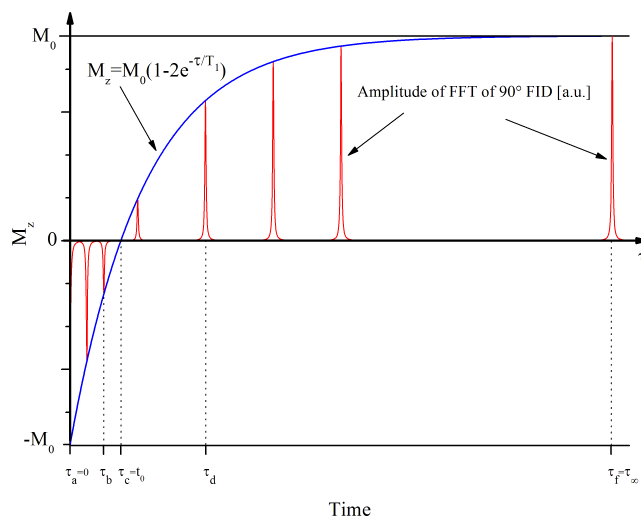
where M_0 corresponds to equilibrium magnetization, such as that recorded at τ_∞ . Note here the additional factor of two relative to equation 2.42 as the recovery starts from inverted magnetization. T_1 is determined by fitting the signal intensities to this equation. This method has the advantage that T_1 can, in principle, be obtained from one measurement. If the magnitude of the 90° pulse FID is zero when $M_z(\tau = t_0) = 0$, then

$$0 = 1 - 2 \exp(-t_0/T_1), \tag{2.53}$$

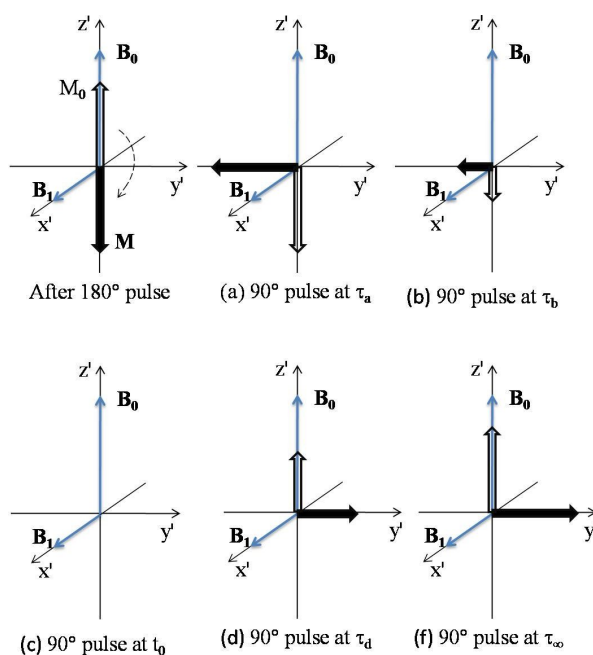
and hence

$$T_1 = \frac{t_0}{\ln(2)}. \tag{2.54}$$

The alternative method of extracting T_1 from such an equation is to analyze a semi-logarithmic plot of $\ln(M_0 - M_z(\tau))$ vs. τ whose slope is $1/T_1$. The most likely causes of error in the use of the inversion recovery method are inaccurate recording of M_0 if full equilibration is not achieved, and inaccuracies in the 180° pulse causing imperfect initial inversion.



(a) Different delays of a 90° pulse and corresponding FFT of the 90° pulse FID.



(b) A 90° pulse after inversion.

Figure 2.12: The inversion recovery pulse sequence.

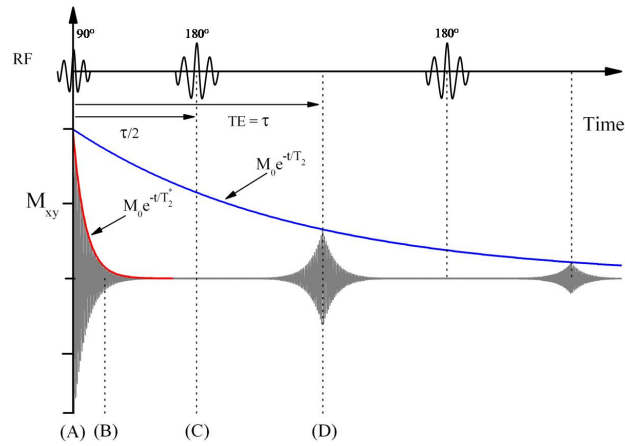
Spin-Echo Sequence

Another commonly used pulse sequence is the spin echo pulse sequence which was proposed in 1950 by Hahn [45] and devised later by Carr and Purcell [46]. This pulse sequence is used to measure the T_2 relaxation time. It consists of a 90° RF pulse to excite the magnetization followed by one or more 180° pulses to refocus the spins to generate signal echoes named spin echoes (SE) as illustrated in Figure 2.13a. First, the 90° pulse is applied to the spin system causing the magnetization to rotate about the x -axis (in the rotating frame) down into the transverse plane. Because of interactions among spins (T_2) and magnetic field inhomogeneities (T_2^*), the transverse magnetization M_{xy} begins to dephase. The moments vectors will fan out in both directions away from the y -axis and will be precessing at slightly different rates as slower components of the magnetization lag and faster components advance.

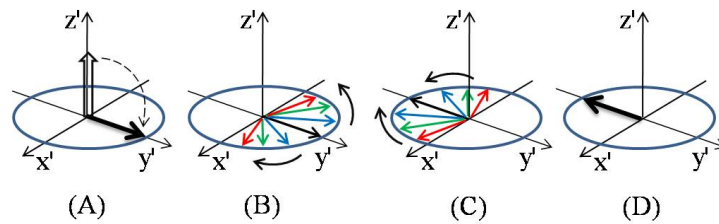
To remove the effect of magnetic field inhomogeneities, a 180° (rephasing) pulse is applied at some time $\tau/2$ after the 90° RF pulse to produce nutation about the x -axis of the rotating frame. This rotates the moments vectors in the xy -plane to the opposite side of the y -axis. The effect of the rephasing pulse is to take spins that were precessing more rapidly and flip them behind the spins rotating at the average rate of precession. Similarly, spins that are rotating more slowly are automatically flipped ahead of the average precession rate. The nuclei are still precessing at different rates because of inhomogeneities in the magnetic field of the system. After the rephasing pulse, the faster spins catch up with the average spins, and the slower spins are caught by the average spins as shown in Figure 2.13b. In this case, the spins are said to have rephased and a measurable signal is produced. This signal is called a spin echo. At the moment of exact rephasing the signal will be strongest since the effect of T_2^* is completely removed. The loss in amplitude of the signal is due solely to any irreversible process and will occur at the time rate of T_2 . The time between the 90° RF pulse and the echo is referred to as time of echo (TE) and is equal to τ . Repeated 90° and 180° pulses with different values of τ can thus be used to measure T_2 . Plotting the intensity against τ , in this case it is a simple exponential decay, and fitting to the following equation gives us T_2 :

$$A(\tau) = M_0 \exp(-\tau/T_2), \quad (2.55)$$

where $A(\tau)$ is the peak amplitude in the NMR spectrum of the echo signal at τ .



(a) Configuration of the spin-echo. A 180° pulse is applied at $\tau/2$ from the 90° pulse, and an echo is formed at $TE = \tau$.



(b) In the spin-echo pulse sequence the 90° pulse (A) causes nutation of the bulk magnetization about the x -axis. Dephasing then occurs (B) as slower components (blue) of the magnetization lag and faster components (red) advance. A 180° rephasing pulse (C) causes nutation about the x -axis and reverses the order of fast and slow components. The components then merge (D) to produce the maximum signal at the negative y -axis. Diagrams A to D are shown in the rotating frame of reference.

Figure 2.13: The spin-echo pulse sequence.

2.2 MRI Contrast Agents

2.2.1 Magnetic Resonance Imaging

Magnetic resonance imaging (MRI) is one of the most powerful imaging techniques for living organisms as it provides images with excellent anatomical details based on soft tissue contrast and functional information in a non-invasive and real-time monitoring manner. The principles of MRI follow from the same principle of exciting spins as found in NMR [47]. In most cases, the MRI machine is tuned to image the most abundant spin population found in the body, that of the protons of bulk water. MRI is a method of constructing images of the body in thin slices. A magnetic resonance image represents a display of spatially localized intensities of water proton signal across the studied slice or volume of the body. Spatial localization is obtained by superimposing on the uniform main magnetic field a spatially varying gradient magnetic field, which essentially tunes the resonance frequencies of each proton according to its position [48].

Contrast in MRI arises from the difference in signal intensities which are represented on the final image as points of relative brightness or darkness in adjacent pixels or voxels. These signal intensities depend on the strength of the magnetic field and the pulse sequence, as well as on certain characteristics that are intrinsic to the tissues being imaged, such as spin-density ρ and the relaxation times T_1 and T_2 . Images can be T_1 -weighted, T_2 -weighted, or proton-density-weighted, and the degree of weighting depends on the pulse sequence, repetition time TR , and echo time TE chosen. For most clinical studies, all three types of images are used because each contributes to the diagnosis of normal and abnormal structures.

The spin-density, proportional to M_0 , reflects the total number of spins available to be imaged within a given tissue (or pixel). In spin-density-weighted imaging, MRI detects signal from water protons. Image is recorded immediately after exciting the system of spins by RF energy followed by a period of spatial encoding. Thus, all spins contribute the same to the signal intensity and picture brightness depends on the spin concentration. In T_1 -weighted imaging, before image recording, the system is kicked out of equilibrium and brought into a new steady state where spins that relax quickly recover more than slowly relaxing spins. Then, the image brightness, in addition to spin density, is weighted by T_1 relaxation rates. In T_2 -weighted imaging, the system is kept initially in equilibrium and the image is recorded some time after perturbation. Spins that have long T_2 relaxation times will contribute more to the signal than spins with short T_2 .

By choosing TR and TE carefully, images can be chosen to favor T_1 , T_2 , or spin-density weighting. The well-known utility of MRI in imaging soft tissue arises from the natural differences in decay rates of various tissues, as in the case of brain imaging where gray and white matter can be easily distinguished. Figure 2.14 shows some examples of the various weighting of typical MRI images.

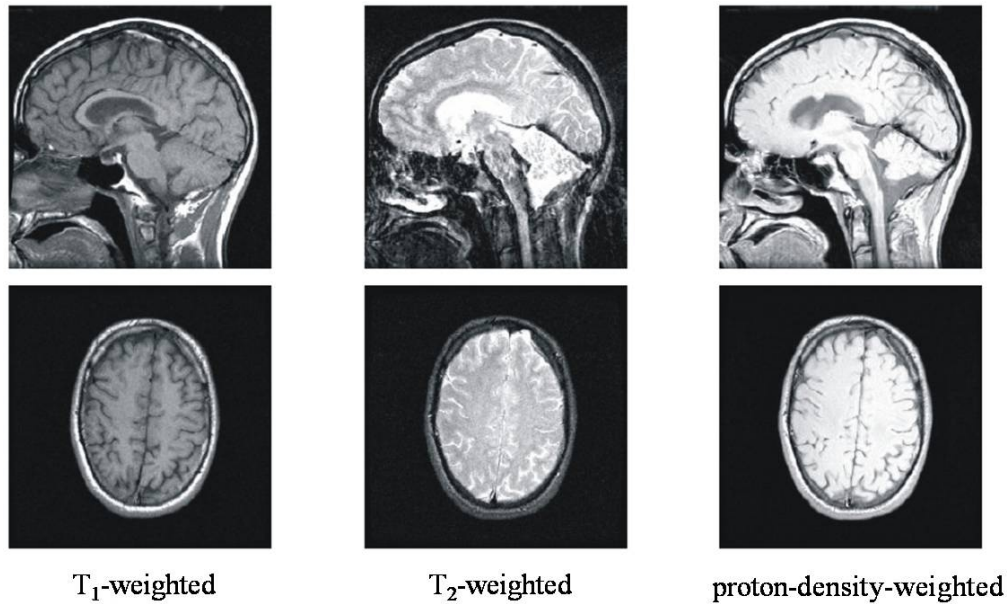


Figure 2.14: Examples of images obtained with different MRI weighting approaches.

Since these are the basic parameters of contrast in the MR image, these parameters should be altered by any potential contrast agent. It is hard to influence the proton density in tissue. Hence, the most effect on changing appearance of different tissues on the MR image is achieved by changing the magnetic relaxation times T_1 and T_2 of the protons in tissue-contained water. Therefore, application of contrast agents (substances) in MRI should change the tissue characteristics.

2.2.2 Contrast Agents

In spite of the excellent soft tissue contrast of MRI, the application of contrast enhancing agents in clinical MRI was proposed already more than 20 years ago [49], and contrast agents are today an integral part of this image modality. MRI contrast agents work by enhancing the relaxation rate of the protons in tissue, thereby altering the signal intensity in the image relative to areas not affected by the contrast agent. The principle of relaxation rate enhancement is as old as NMR itself. Bloch and coworkers published already in 1946 how the addition of paramagnetic ions such as $\text{Fe}(\text{NO}_3)_3$ enhanced the relaxation rate of water protons [50]. The addition of paramagnetic ions to pure water results in an increase of the relaxation rates R_1 and R_2 which are directly proportional to the concentration of the paramagnetic species.

A contrast agent in MRI can be thought of as a catalyst that decreases the proton relaxation times of tissue water. In contrast enhanced MRI, the effect of the agent on proton relaxation is observed; not the contrast agent directly. Contrast agents in MRI can for example be administered to further enhance tissue contrast, to characterize lesions, and to evaluate perfusion and blood flow abnormalities [51]. They can be divided into different classes according to their magnetic properties, *in vivo* relaxation effects and biodistribution: agents that influence mainly the signal in T_2 -weighted images (negative contrast agents, reducing the signal) or in T_1 -weighted images (positive contrast agents, increasing the signal).

Paramagnetic Agents

Paramagnetic agents contain water-soluble metal ions with one or more unpaired electrons. The most common paramagnetic metal used as an MRI contrast agent is gadolinium (Gd^{3+}) which has seven unpaired electrons [52]. For *in vivo* use, the gadolinium ions must be chemically linked to a carrier molecule, called a ligand, to reduce toxicity and alter the pharmacokinetic properties of the metal. The resulting gadolinium containing molecule is referred to as a chelate. Gadolinium (Gd^{3+}) chelates accelerate longitudinal (T_1) relaxation of water protons and exert bright contrast in regions where the complexes localize [53].

Superparamagnetic Agents

Superparamagnetic contrast agents are composed of a water insoluble crystalline magnetic core, usually magnetite (Fe_3O_4) or maghemite ($\gamma\text{-Fe}_2\text{O}_3$). The mean core diameter normally ranges from 4 – 10 nm, and the core is surrounded by polymer coating, often dextran, polyethyleneglycol or ionic sheath. Dextran coated iron oxides are essentially biocompatible, since any iron left when the particles break down can be recycled naturally by the human body.

These crystals are often referred to as magnetic nanoparticles (MNPs), and each nanoparticle contains several thousand paramagnetic Fe ions (Fe^{2+} or Fe^{3+}). If the Fe ions are magnetically ordered within the crystal, the net magnetic moment of the nanoparticle is so large that it greatly exceeds that of typical paramagnetic ions [54]. The total size of the particle is expressed as the mean hydrated particle diameter. Iron oxide nanoparticles are commonly sub-divided into two groups, depending on the overall size of the particle. Nanoparticles with a total particle size less than about 50 nm are referred to as ultra-small particles of iron oxide (USPIO), whereas particles with a total size in the range of 50 – 200 nm are referred to as small particles of iron oxide (SPIO).

MRI contrast agents based on SPIO and USPIO particles have already been approved for clinical use. Iron oxides were first used for *in vivo* nuclear magnetic resonance experiments in 1978 [55]. Over the following few years several investigators reported on the use of iron oxide preparations as potential MRI contrast agents [56]. Iron oxides primarily decrease T_2 relaxation times (T_2 agents) and decrease signal intensity of tissue (hypointense tissue), an effect most pronounced on T_2 -weighted pulse sequences [57, 58]. Longitudinal (T_1) relaxation is generally less affected by this class of agents because of its lack of contribution to the rotational motion.

2.3 Ultrasound

Ultrasound is simply a sound wave, like audible sound. Although some physical properties are dependent on the frequency, the basic principles are the same. The audible range of sound frequencies for humans is 20 Hz to 20 kHz, while diagnostic US is in the range of 1 – 12 MHz. In homogeneous, isotropic materials US waves propagate in straight forward manner. In solid materials wave propagation can be either longitudinal or transversal. In liquids and gases wave propagation is longitudinal because there are no solid structures that could conduct vibrations to perpendicular direction. US waves propagate through a medium by the vibration of molecules (longitudinal waves). Within the wave, regular pressure variations occur with alternating areas of compression that correspond to areas of high pressure and high amplitude, and with areas of rarefaction or low pressure zones where widening of particles occurs as shown in Figure 2.15.

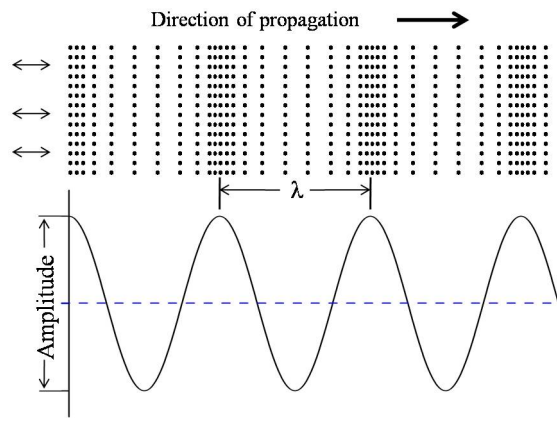


Figure 2.15: Longitudinal wave.

2.3.1 Characteristics of Ultrasound

Propagation velocity (c) is the speed at which US waves propagate through a medium, and it is related to the frequency ν and the wavelength λ of US wave as:

$$c = \nu\lambda. \quad (2.56)$$

The frequency of US waves is determined by the source of the acoustic vibrations. The speed of US depends on what material it is traveling in. It depends principally on the density (ρ) and the compressibility (κ) of the medium.

$$c = \sqrt{\frac{1}{\rho\kappa}}. \quad (2.57)$$

A medium with high compressibility yields a slow US velocity and vice versa. Hence, the velocity is relatively low in gases, intermediate in liquids, and greatest in solids. The sound velocity in a given medium is constant (at a given temperature), but varies in different materials as shown in Table 2.1.

The velocity of an US wave (c) should be distinguished from the velocity of molecules (v) whose displacement into zones of compression and rarefaction constitutes the wave.

The molecular velocity describes the velocity of the individual molecules in the medium, whereas the wave velocity describes the velocity of the US wave through the medium. Properties of US such as reflection, transmission, and refraction are characteristic of the wave velocity rather than the molecular velocity.

Acoustic vibrations propagating in a medium create a pressure known as the acoustic pressure [59] which is written as:

$$p = p_0 \sin(\omega t), \quad (2.58)$$

where p is the acoustic pressure at any instant, and p_0 is the acoustic pressure amplitude. The acoustic pressure of a plane progressive wave is related to the molecular velocity by

$$p = vZ, \quad (2.59)$$

where Z is the specific acoustic impedance of the material and defined as the product of its density (ρ) and acoustic velocity (c).

$$Z = \rho c = \sqrt{\frac{\rho}{\kappa}}. \quad (2.60)$$

The specific acoustic impedance connects the acoustic pressure amplitude (p_0) in the medium with the US wave intensity (I) by the following expression [60]:

$$I = \frac{p_0^2}{2\rho c} = \frac{p_0^2}{2Z}. \quad (2.61)$$

Acoustic impedances of several materials are listed in Table 2.1. Acoustic impedance is important for determination of acoustic transmission and reflection at the boundary of two materials having different acoustic impedances, designing of ultrasonic transducers, and assessing absorption of sound in a medium.

Material	c [m/s]	ρ [kg/m ³]	Z [kPa.s/m]
Air at STP	333	1.2	0.4
Water	1480	1000	1480
Quartz Glass	5570	2600	14482
Aluminum	6320	2700	17064

Table 2.1: Approximate Velocities of US and Acoustic Impedances of Selected Materials [61].

2.3.2 Production of Ultrasound Waves

US waves are produced by a transducer. A transducer is a device that takes power from one source, converts the energy into another form, and delivers the power to another target. In this case the transducer converts electrical signals to US waves, and picks up the reflected waves converting them back into electrical signals. US transducers are made from quartz crystals or ceramic with piezoelectric properties. This material vibrates at a resonant frequency when an alternating electric current is applied. When an electrical

current is applied to this material, its shape changes with polarity. This causes expansion and contraction that in turn leads to the production of compression and expansion of sound waves. Conversely, this material emits electrical currents when it changes dimensions as a result of an imposed mechanical force. The same crystals can be used to send and receive sound waves. This phenomenon is known as the piezoelectric effect. Piezoelectricity was discovered by Jacques and Pierre Curie in the 1880 during experiments on quartz.

The active material of most acoustic transducers used today is a piezoelectric ceramic, which can be cut in various ways to produce different wave modes. Preceding the advent of piezoelectric ceramics in the early 1950's, piezoelectric crystals made from quartz crystals (SiO_2) were primarily used. Development of piezoelectric devices and materials led to the discovery of a new class of materials, called ferroelectrics, which exhibited piezoelectric constants many times higher than natural materials. All ferroelectric materials are piezoelectric, however, not all piezoelectric materials are ferroelectric. Below a transition temperature called the Curie temperature ferroelectric materials are polar and possess a spontaneous polarization or electric dipole moment. However, this polarity can be reoriented through the application of an electric field. The non-polar phase encountered above the Curie temperature is known as the paraelectric phase.

When ferroelectric ceramics were introduced, they soon became the dominant material for transducers due to their good piezoelectric properties. The first piezoceramic in general use was barium titanate (BaTiO_3), and that was followed during the 1960's by lead zirconate titanate (PZT) compositions. PZT is a ceramic perovskite material that shows a marked piezoelectric effect, and it is now the most commonly employed ceramic for making transducers. The ferroelectric Curie temperature of PZT is about 320°C and is dependent on the composition. Figure 2.16 shows the crystal structure of a traditional piezoelectric ceramic.

Frequency is a specific feature of the crystal used in the US transducer. A crystal exhibits its greatest response at the resonance frequency which is determined by the thickness of the crystal. The most efficient operation is achieved for a crystal with a thickness equal to half the wavelength of the desired US. A crystal of half-wavelength thickness resonates at a frequency ν :

$$\begin{aligned}\nu &= \frac{c}{\lambda} \\ &= \frac{c}{2t},\end{aligned}\tag{2.62}$$

where $\lambda = 2t$, and t is the thickness of the crystal. High frequency US transducers employ thin ($< 1\text{ mm}$) piezoelectric crystals. A thicker crystal yields US of lower frequency. For an US wave incident perpendicularly upon an interface, the fraction of the incident energy that is transmitted across the interface is described by the transmission coefficient σ_T :

$$\sigma_T = \frac{4Z_1Z_2}{(Z_1 + Z_2)^2},\tag{2.63}$$

where Z_1 and Z_2 are the acoustic impedances of the two media. If $Z_1 = Z_2$, σ_T is maximum. The fraction of the incident energy transmitted across an interface depends

on the difference in acoustic impedance of the media on opposite sides of the interface. With a small impedance mismatch at an interface, much of the energy of an US wave is transmitted, and only a small amount is reflected from the interface. For example, an interface consisting of aluminum and quartz glass on each side has a high transmission coefficient, $\sigma_T = 0.99$.

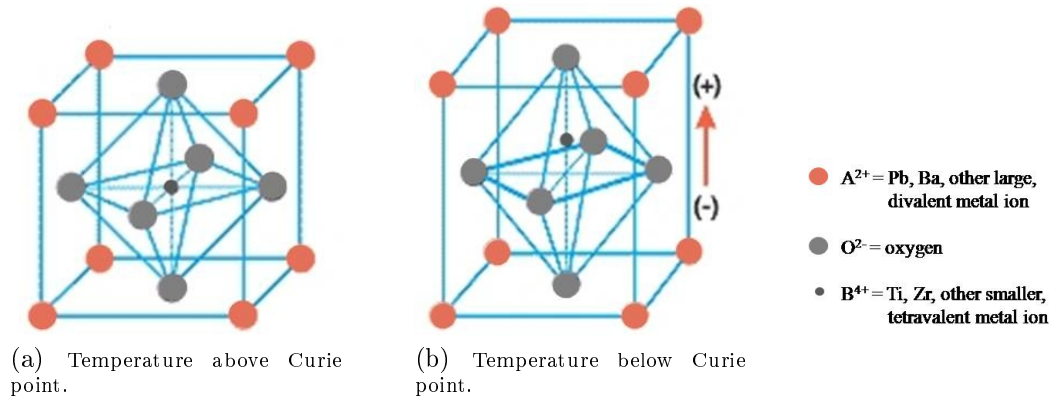


Figure 2.16: Crystal structure of a traditional piezoelectric ceramic. (a) Cubic lattice, symmetric arrangement of positive and negative charges. (b) Tetragonal (orthorhombic) lattice, crystal has electric dipole.

Chapter 3

Method

3.1 Principle

In a standard proton NMR experiment an external constant magnetic field \mathbf{B}_0 polarizes the spin system to some extent, and an equilibrium magnetization M_0 is reached. If the magnetization is perturbed with an adequate RF pulse, M_0 recovers exponentially with the spin-lattice relaxation time T_1 . The recovery process is dominated by stimulated transitions of the nuclear magnetic moments between their Zeeman energy states, hence T_1 is a direct measure for the spectral density at the protons' Larmor frequency ν_0 .

Let us now consider magnetic nanoparticles (MNPs) to be homogeneously distributed in a water sample as a colloidal solution. Apart from some thermal fluctuations their magnetic moments align along \mathbf{B}_0 . Since a fraction of these fluctuations contribute to the spectral density at ν_0 , T_1 of the solution can be adjusted nearly arbitrarily by changing the concentration of MNPs.

Now, if an aqueous solution of MNPs is subjected to a longitudinal ultrasonic wave having a wavelength about 10^3 times greater than the nanoparticle diameter, MNPs will be accelerated periodically by the movement of the surrounding medium. This results in a translational movement of the MNP which hardly affects T_1 of the solvent even if the US frequency ν_{US} matches ν_0 [12].

Nevertheless, if the MNP is conjugated to a molecule, such as an antibody, forming an asymmetric magnetic nanoparticle (AsMNP), an additional motion is expected to be initiated which does affect T_1 of the solvent. In this case, asymmetry of the particle is achieved by attaching a biotinylated antibody to a streptavidin coated magnetic nanoparticle from one side only so that the center of mass of the AsMNP is different from its center of geometry. In magnetic resonance imaging, antibody coated MNPs are commonly used as contrast agents [62]. The non-covalent bond formed between biotin and avidin or streptavidin is a very tight interaction [63]. This strong interaction approaches the strength of a covalent bond. Figure 3.1 shows the attachment of a biotinylated antibody with a streptavidin coated MNP. In this figure one antibody is shown attached to the MNP. This does not mean that only one antibody is attached. Attachment of antibodies to the MNP depends very much on how many spots of streptavidin coatings at the MNP's surface there are. However, streptavidin coatings at the bottom surface of the MNP will not be attached to antibodies. The processes of the AsMNPs preparation are explained in the next section.

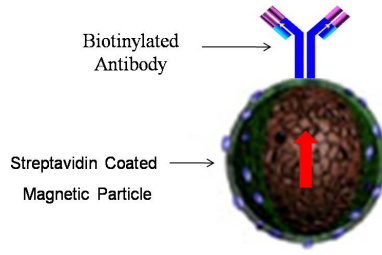


Figure 3.1: Attachment of a biotinylated antibody to a streptavidin coated magnetic nanoparticle (Courtesy of Molecular Vision 2006; **12**, 616-625).

Because the antibody accelerates differently in the ultrasonic wave than the MNP, it causes a torque acting on the MNP's surface. Therefore, the MNP will tilt periodically by a small angle as shown in Figure 3.2. Due to the crystal anisotropy, the magnetization is coupled to the particle. Its amplitude and direction will change due to the resulting tilting of the MNP. Accordingly, these AsMNPs act as US-driven RF antennas, emitting radio waves with US frequency which can be received by the nuclear magnetic moments of the solvent. If $\nu_0 = \nu_{US}$, protons of the solvent in the near field region of the AsMNP are stimulated to emit energy and the spin-lattice relaxation time T_1 of the aqueous solution will decrease. Because the US wavelength λ_{US} is short compared to the sample dimensions, these radio frequencies are effective in the near field region of the particle, and cancel out in the far field.

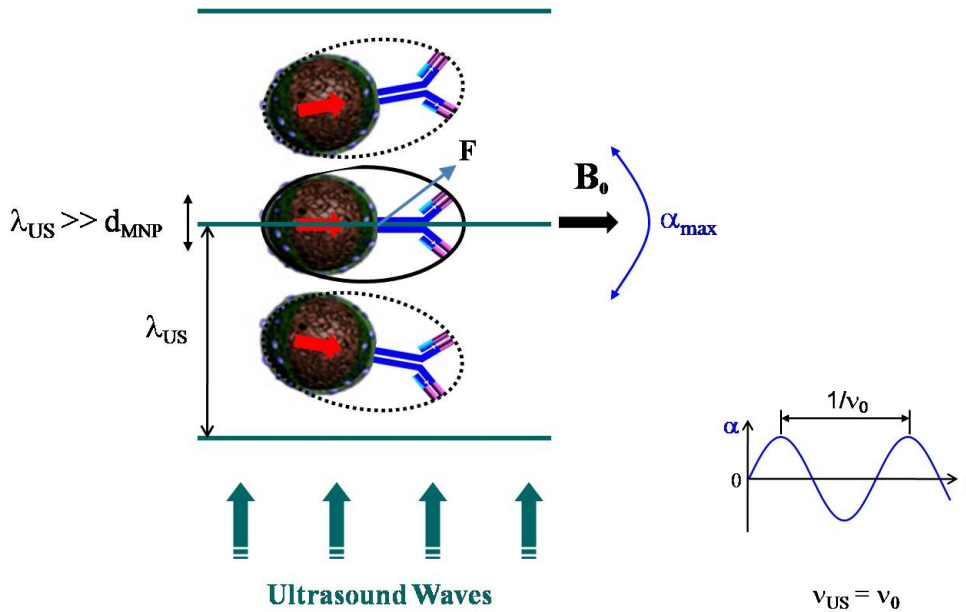


Figure 3.2: Application of US to a sample containing the asymmetric magnetic nanoparticles (AsMNPs). Both the MNP and the antibody accelerate periodically. Because the antibody has a smaller density, it is moving with a greater amplitude than the MNP is, and causing a force at the MNP surface. λ_{US} is the US wavelength, d_{MNP} is the MNP diameter, $\theta = \alpha_{max}$ is the tilting angle.

Tilting Angle

The following is a rough estimate of the tilting angle of the asymmetric magnetic nanoparticles caused the application of US in the aqueous solution . The oscillation amplitudes of the magnetic particle and the antibody are computed using a simple model taking into account a sound pressure of $p = 7.4 \times 10^4$ Pa in distilled water [64] and the maximum particle velocity to be $v_0 = p/z = 5.0 \times 10^7$ nm/s. The motions of the MNP and the antibody are treated separately. Therefore, the equation of motion of each particle in the solution subjected to US wave is given by

$$m\ddot{x} + \zeta\dot{x} = \zeta v_0 \cos(\omega t), \quad (3.1)$$

where m denotes the particle mass, $\zeta = 6\pi\eta r$ is Stokes drag coefficient, η is the liquid viscosity. and r is the particle hydrodynamic radius. The oscillation amplitude a of each particle can be computed by solving equation (3.1)¹. The tilting angle θ is defined as $\theta = \Delta a/d$, where Δa is the difference in the oscillation amplitudes, and d is the distance between the centers of masses of the antibody and the magnetic particle when coupled to the AsMNP. The tilting angle of an asymmetric magnetic nanoparticle consisting of one MNP and one antibody attached in the same configuration shown in Figure 3.1 is $\theta = 4.3 \times 10^{-4}$ degrees at the Larmor frequency ν_0 in this setup.

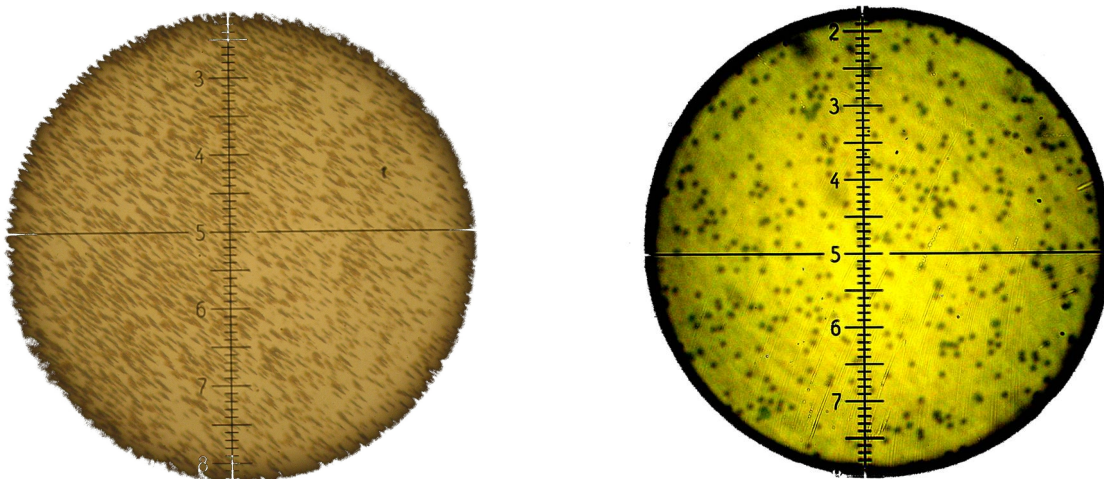
However, it is worth mentioning that the number of antibodies attached to the MNP is not known. That depends very much on how many streptavidin coating sites there are at the MNP's surface. In addition, the configurations of the attachments with respect to the direction of the magnetic moment of the MNP are not the same for all AsMNPs.

¹Oscillation amplitude $a = \frac{v_0 \lambda^2}{\omega(\lambda^2 + \omega^2)}$ with the characteristic frequency $\lambda = \zeta/m$. $r_{MNP} = 25$ nm, $r_{Anti} = 4$ nm, $\eta = 1$ g m⁻¹ s⁻¹, $m_{MNP} = 9.2 \times 10^{-17}$ g, $m_{Anti} = 2.5 \times 10^{-19}$ g.

3.2 Sample Preparation

As mentioned earlier in the principle, the asymmetric particle is composed of magnetic nanoparticle (MNP) and antibody. The density of the MNP is greater than the density of the antibody. To make the attachment of the antibody to the MNP from one side only, sedimentation of the MNP is necessary before making the chemical reaction for attachment. The MNP could be held fixed to the bottom surface of the reaction container using a rare-earth magnet. This idea was tested, but the problem was that some MNPs were clustered on top of each other forming needles. Figure 3.3a is a microscopic picture of $1.3\ \mu\text{m}$ magnetic particles (MPs) forming needles when a sedimentation is done just by placing a rare-earth magnet directly below the sample container. This formation makes it unsuitable for antibody attachment. More pictures are presented in Appendix A.

However, if the MNPs are separated and sedimented initially by a centrifugal force, and then a magnetic force is used to hold the particles fixed to the bottom surface, needles will not be formed. In the beginning the centrifugal force causes the MNPs to be distributed randomly at the bottom surface as a monolayer and not on top of each other. Increasing the centrifugal force will lead to holding the MNPs at the bottom. Then the container is accelerated slowly by this force to be placed on a magnet that can hold the MNPs after removing the centrifugal force. The chemical reaction of the antibodies and the MNPs takes place while the sample container is on the magnet. The magnet not only ensures that the MNPs do not get clustered but also that their magnetic moments are in the same direction. Figure 3.3b shows a microscopic picture of the same MNPs shown earlier which are sedimented by application of a centrifugal force and then by a magnetic force. More pictures are presented in Appendix A. As seen in the picture, the MNPs are distributed randomly and no needles are formed. After this sedimentation the reaction can take place and asymmetry of the particles can be achieved. Next is a detailed procedure of how the sedimentation took place, what tools are used for that, and the steps of the chemical reaction.



(a) Sedimented magnetic particles using only a rare-earth magnet. The magnetic particles are forming needles. Distance between small graduation lines is $10\ \mu\text{m}$.

(b) Sedimented magnetic particles by a centrifugal force and by a magnetic force. No needles were observed in this process. Distance between small graduation lines is $2\ \mu\text{m}$.

Figure 3.3: Microscopic pictures of sedimented $1.3\ \mu\text{m}$ magnetic particles.

3.2.1 Experimental Setup for Sedimentation

In this work two sizes of MNPs and two antibody isotypes are used for the chemical reactions. Avidin coated magnetic particles² with a diameter of $d_{MNP} = 1.3 \mu\text{m}$ reacted with biotin conjugated affinity purified anti-chicken IgM³ with a molecular mass of approximately 900 kDa. Streptavidin coated MNPs⁴ with a diameter of $d_{MNP} = 50 \text{ nm}$ reacted with biotin conjugated affinity purified anti-chicken IgG⁵ with a molecular mass of approximately 150 kDa. Specifications of these products are given in Appendix B. The big magnetic particles ($1.3 \mu\text{m}$) were used so that they can be easily seen under the microscope whether they were successfully sedimented or not. The sedimentation process and the chemical reaction that are explained here are for the 50 nm MNPs and the IgG antibody. Figure 3.4 shows the experimental setup that was used for the sedimentation process of the MNPs.



Figure 3.4: Experimental setup for sedimentation process of the MNPs. It consists of a centrifuge, a transformer, a cylindrical tool, and a sample vessel.

The 50 nm MNPs were provided in 1 ml solution with a concentration of 2.5 mg/ml. This solution was diluted in buffer (0.02 M KH_2PO_4 , 0.15 M NaCl, at pH 7.0) to obtain a dilution with a concentration of 5.12×10^{-3} mg/ml. The IgG antibody was provided in a 1 ml solution with a concentration of 1 mg/ml. This solution was diluted in the same buffer to obtain a dilution of the antibody with a concentration of 1.08×10^{-3} mg/ml. Also, a biotin wash solution was prepared with the same buffer to be used later to stop the chemical reaction of the antibodies with MNPs.

²Spherotech, Inc.

³Rockland Immunochemicals, Inc.

⁴micromod Partikeltechnologie GmbH.

⁵Bethyl laboratories, Inc.

3.2.2 Sedimentation Process

A sample of 300 μl of the MNPs dilution was used for sedimentation. It was put into the vessel shown in Figure 3.5. This vessel was made of aluminum with a thickness of 0.5 mm, a height of 11 mm, and an inner diameter of about 11 mm. A glass disc of thickness 1 mm and a diameter of about 11 mm was glued at the inner bottom surface of the vessel.



Figure 3.5: Sample vessel is made from aluminum with a lid (white) made from Polyoxymethylene (Delrin). A glass disc is glued on the inside bottom surface of the vessel.

After closing the vessel with the lid shown in white in the picture, it was inserted from the open top in the cylindrical tool shown in Figure 3.7. The cylinder was already filled with water to a height of about 26 mm. The dimensions of the vessel were carefully constructed such that the vessel plus the amount of the sample have a buoyancy that is greater than their own weight. Therefore, the sample vessel floated on the surface of the water. The sample was at a height of 32 mm far from the magnet where its magnetic field was measured to be 2.84 mT. It is too small to affect the alignment of the magnetic moment of the MNPs. Figure 3.6 shows the relation between the magnetic field of the rare-earth magnet and the height from the surface of the magnet. In the figure, positions of the sample when the vessel was floating (32 mm), and when water was removed (4 mm) are marked with red and green lines, respectively.

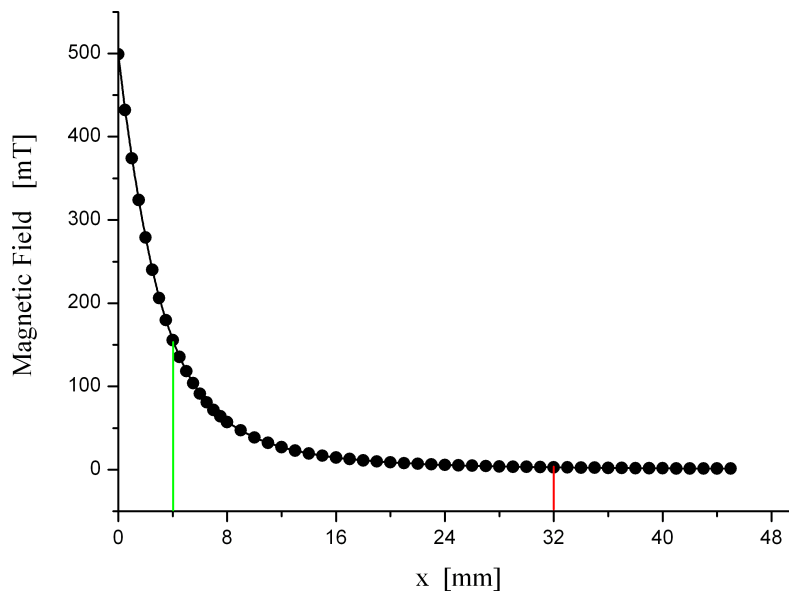


Figure 3.6: The relation between the magnetic field of the rare-earth magnet and the height (x) above the magnet. Starting position is at 32 mm marked with red. Final position is at 4 mm marked with green.



Figure 3.7: A cylindrical tool used for sedimentation of the MNPs initially by a centrifugal force and then by a magnetic force. It consists of a screw, a spring, a rare-earth magnet, and an open cylinder with a small cut used as a hook. The cylinder is filled with water to a height of 26 mm. If the centrifugal force is strong enough to compress the spring down, the water will leak from an opening made above the magnet. The purpose of the screw is to adjust the elasticity of the spring.

Then, this tool is fastened on the centrifuge with a hook as shown in Figure 3.8. The machine is connected to a transformer for controlling the voltage. It is initially set to start working for 3 h at 130 V (1200 r/min). This voltage was chosen after a few attempts to make sure that the spring in the cylindrical tool was not compressed allowing water leak from the cylindrical tool. After three hours the voltage was increased to 220 V (3000 r/min). The corresponding relative centrifugal force (RCF) acting on the spring was strong enough to compress it leading to water leakage. The centrifuge was left running at this voltage for about 15 min to make sure that all water had leaked and the sample vessel was driven to be placed on the magnet. After this process the MNPs were sedimented and fixed to the bottom surface as a monolayer. A picture of sedimented $1.3 \mu\text{m}$ magnetic particles was shown previously.



Figure 3.8: The Centrifuge. As seen, there are two cylindrical tools that are hooked. Each contains a rare-earth magnet inside. The magnets are used to repel each other so that the sample vessel rotates uniformly around the axis at the center.

3.2.3 Final Preparation of Sample

Before starting the chemical reaction steps, 120 μl solution was removed from the top surface of the sample. T_1 of this solution was experimentally determined and found to be very close to T_1 of water. This ensures that the particles are sedimented and fixed at the bottom surface. To proceed with the chemical reaction, 200 μl of the prepared IgG antibody dilution were added to the remaining sample. After adding the antibody, the sample was left overnight for the completion of the chemical reaction. Note that the sample vessel was kept on the magnet to ensure that reaction did not occur from all sides of the MNP. The next day, 200 μl solution were removed from the top surface of the sample. Then, about 300 μl of the biotin wash solution was added and the sample vessel was still on the magnet. After 5 h, about 220 μl solution were removed from the sample, and the sample vessel was removed from the magnet. Finally, 160 μl of the biotin wash solution was again added, and the sample was mixed for about 5 min. Then, the sample of the aqueous solution with suspended AsMNPs was ready to be used for measurements. Some of the buffer was added later to raise the T_1 of the sample for measurement purposes.

Chapter 4

Experimental Setup

In order to verify the concept presented in the previous chapter experimentally, the following experimental setup was built. The experimental setup can be divided into two areas: NMR electronics and US electronics.

4.1 NMR Electronics

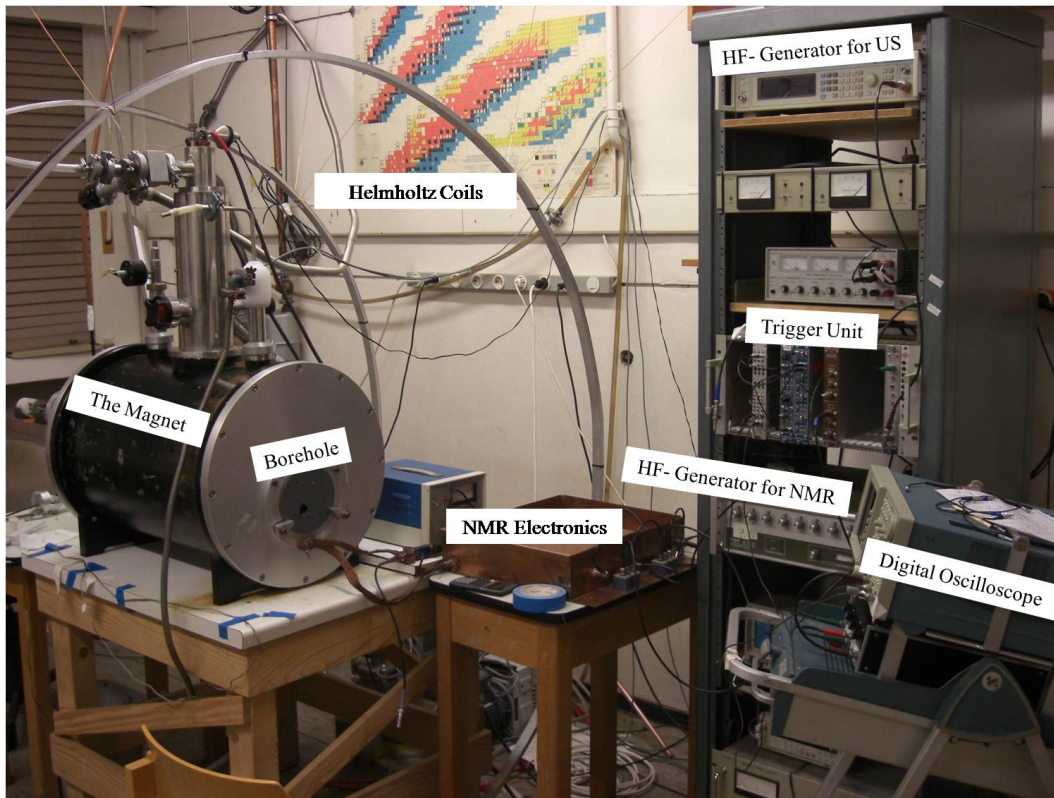
4.1.1 The Magnet

The production of the constant magnetic field \mathbf{B}_0 is achieved by an NMR spectrometer¹ with a superconducting solenoid. The spectrometer in Figure 4.1 has a length of about 680 mm with a room temperature borehole of 75 mm diameter and a two-stage helium-nitrogen cooling. The solenoid is located in a helium cryostat, where it is permanently cooled by liquid helium (boiling point of 4.2 K). This inner tank is surrounded by a tank filled with liquid nitrogen (boiling point of 77.4 K). Both tanks are isolated by a vacuum tank. The magnetic field can be set from 0 T to 5 T. The Larmor frequency of the aqueous samples used in this setup was about 18.26 MHz which corresponds to a magnetic field of about 0.43 T. The homogeneity of the magnetic field is optimized by manual shimming, and it can be achieved to be less than 0.1 ppm.

4.1.2 Helmholtz Coils

Although a superconductor is used to generate the \mathbf{B}_0 field, there is a decrease in the magnetic field strength slowly with time. This decrease is mainly due to ohmic losses at the bridge contact between the superconducting coils. These ohmic losses in the superconducting contacts decrease the flow of electricity stored in the magnet which in turn causes the magnetic field to decrease. The drift in the Larmor frequency is about 200 Hz/h. For comparable results, it is important to work at a constant Larmor frequency. To compensate for this frequency drift, Helmholtz coils were installed around the magnet. They are symmetrically placed around the sample volume. The Helmholtz pair has a mean diameter of 1.9 m and a distance of 0.8 m, and each is made of 12 windings. The maximum current that can pass through the Helmholtz coils is 40 A.

¹Oxford Instruments Ltd.



(a) NMR spectrometer.



(b) NMR transmission electronics.



(c) NMR receiving electronics.



(d) The probe.

Figure 4.1: The experimental setup for the NMR spectrometer and electronics. The probe sample is inserted from the opposite side of the borehole. The cable used for NMR signals is connected to the sample probe from the seen side. The cables used for US signal and interference antenna are connected from the opposite side. The best homogeneity of the magnetic field of the borehole is exactly in the middle. Pieces of metal sheets were used for shimming the magnet from outside to improve the homogeneity. Helmholtz coils were installed to compensate for the magnetic field drift.

A computer program is used to increase the current in the Helmholtz pair with time. The resulting Larmor frequency is balanced within an error of 1.5 Hz. Figure 4.1 shows a picture of the NMR spectrometer, the Helmholtz coils, the transmission and receiving electronics, and the sample probe.

4.1.3 Signal Processing Electronics

Figure 4.2 shows a schematic diagram of the electronics used for the NMR spectroscopy. The NMR electronics can be divided into two branches. The first branch (shown in blue) is used to show the transmission electronics to produce the RF pulses. The second branch (shown in red) is used to process the received signal from the sample probe. The high frequency generator² produces a sine wave with the specified frequency for the NMR spectroscopy. This signal is divided in the splitter so that later it can be mixed with the received signal.

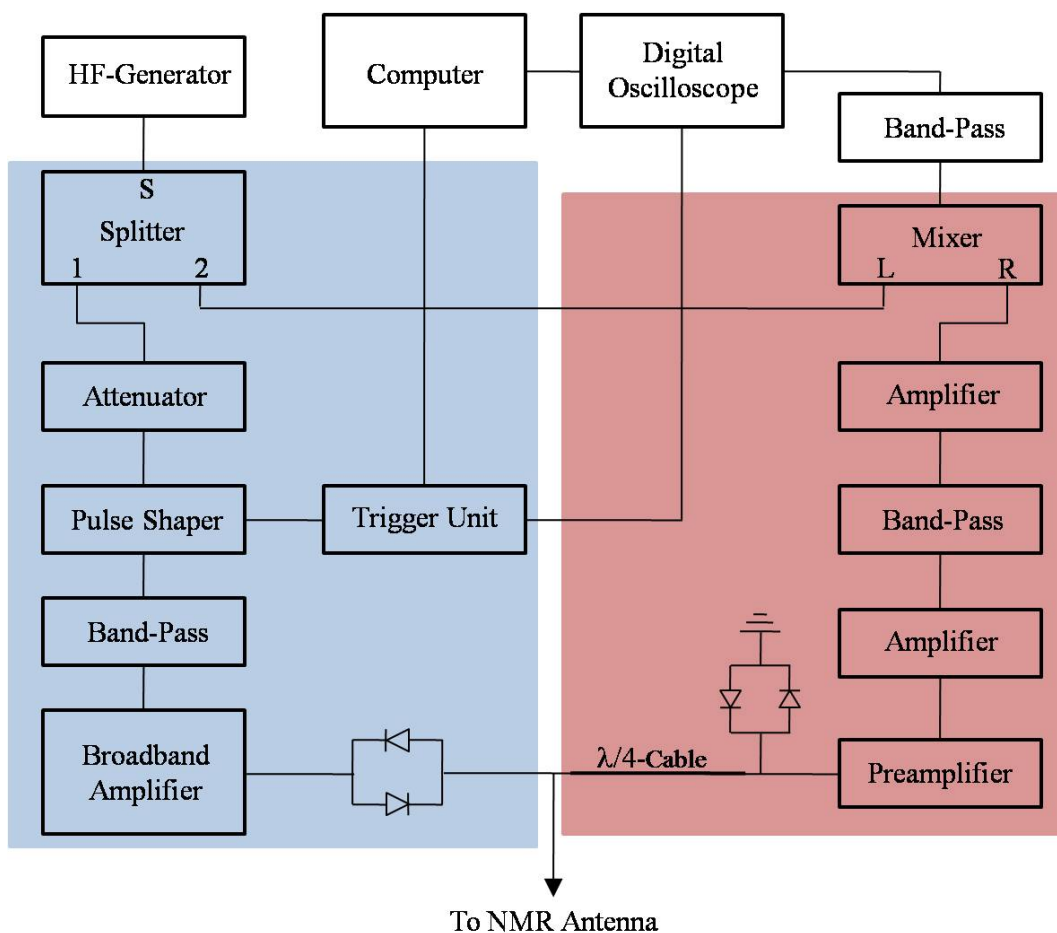


Figure 4.2: A schematic diagram of the NMR electronics: Light blue is the transmission electronics. Light red is the receiving electronics.

In the first branch, the signal is initially passed through an adjustable attenuator and then goes through a triggered pulse shaper to obtain an envelope of a rectangular shape of the specified pulse length. The lengths of the 90° and 180° pulses are adjusted in time

²PTS 250.

units according to equation (2.37). If a typical 90° pulse has a length of $12 \mu\text{s}$, a 180° pulse would be twice as long. The pulse shaper is connected by a trigger unit which is triggered by computer. The pulse shaper transmits the signal through a band-pass filter. The band-pass filter provides a reduction of noise so that in the broadband amplifier it does not get amplified. After the pulse shaper, the pulsed signal is about $15 V_{\text{pp}}$ which is amplified by the broadband amplifier even up to $60 V_{\text{pp}}$. At the output of the amplifier, crossed diodes are used to allow the large signal to pass through and block low amplitude signals. The signals received from the sample probe, however, are blocked by the diodes. Their amplitude is too small to pass through the diodes.

The received signals initially pass to a preamplifier through a $\lambda/4$ -cable. Then, they go through several amplifier stages where at each additional stage amplification is increased by 17 dB. A pair of grounded crossed diodes are located at the entrance of the sensitive preamplifier to protect it from the high levels of the broadband amplifier. This high amplitude signal from the transmitting unit is short-circuited at the pair of the grounded crossed diodes and reflected with a 180° phase shift. The $\lambda/4$ -cable is used to ensure that high amplitude signals interfere destructively with the reflected signals from the pair of diodes. The low amplitude signal will encounter a 50Ω resistor as they go into the preamplifier.

Between the amplifier stages the received signals go through a band-pass filter so that even at this point the noise is reduced again. The amplified signal is then fed to the mixer, where it is mixed with the diverted signal by the splitter at the beginning portion of the transmitter signal. A mixer can be understood as an analog multiplier. If two frequencies $\cos(\omega_1 t)$ and $\cos(\omega_2 t)$ at the inputs of the mixer are turned on, the mixer trigonometrically converts the product to two splitted frequencies as:

$$\cos(\omega_1 t) \cdot \cos(\omega_2 t) = 1/2 \cos[(\omega_1 + \omega_2)t] + 1/2 \cos[(\omega_1 - \omega_2)t]. \quad (4.1)$$

So, the mixer gives the sum of both frequencies and their difference. Therefore, the amplified megahertz signal of the sample probe and the megahertz signal from the RF generator are converted down by their difference to a few kilohertz. The mixing frequency is a few kilohertz higher than the Larmor frequency. Another band-pass filter is set at the difference frequency. After passing through the band-pass, the signal is digitalized, displayed at a digital oscilloscope³, and recorded by a computer where it can be analyzed.

4.1.4 Sample Probe

The NMR antenna, which is in the sample probe, sends RF energy into the sample and detects the received signal from the sample. The pulses of the transmitter unit are sent through a coaxial cable to the sample probe. The sample probe which is shown in Figure 4.3 is made of an aluminum box that contains the NMR antenna and the sample holder.

The coil of the NMR antenna is a solenoid of $N = 10$ loops, a length of approximately $l = 14.5 \text{ mm}$, and radius of about $r = 4.2 \text{ mm}$. Thus, the coil has an inductance of about $4.8 \times 10^{-7} \text{ H}$. The inductance was calculated using the following formula:

³Tektronix TDS 744A.

$$L = \frac{\mu_0 N^2 \pi r^2}{l}. \quad (4.2)$$

The coil which has a fixed inductor is connected in parallel with the capacitor C_1 to set the resonant frequency of the resonant circuit as shown in Figure 4.3. The capacitor C_1 is composed of two parallel capacitors: the first has a constant capacity of 132.3 pF, and the second can be regulated between 10 and 40 pF. The capacitor C_2 in the NMR antenna optimizes the resonance frequency of the circuit. The resonant circuit is tuned to a resonance frequency of 18.26 MHz which is adapted to the resonance frequency of the US system.

The sample is contained in a sample holder made of teflon which is placed centrally in the NMR coil. Volume of samples used in the spectroscopy was 100 μL . The teflon holder had an inside diameter of about 5.8 mm which resulted in a sample height of about 3.8 mm.

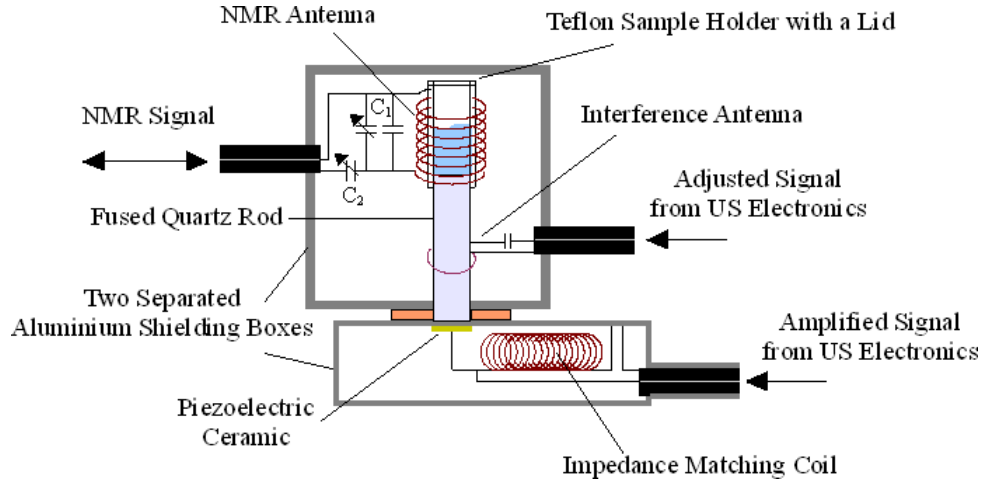


Figure 4.3: Sample probe is made of two aluminum shielding boxes. The lower box is for the US emitter. The upper box contains the NMR antenna and the sample holder. The liquid sample (shown in blue) is placed in the volume ($\phi \times h = 5.8 \text{ mm} \times 3.8 \text{ mm}$) on top of the fused quartz rod that is used for transferring US waves to the sample.

The resonant circuit has a measured quality with approximately 40, and the filling factor of the coil was calculated to be about 0.11 using:

$$\text{Filling Factor} = \frac{\text{Volume of Sample}}{\text{Volume of Coil}}. \quad (4.3)$$

4.2 Ultrasound Electronics

A high frequency generator⁴ is used to obtain the radio frequency signals needed for US waves. The frequency generator could be triggered by computer to give a pulsed signal of a specified length at a certain time delay. These signals from the generator are splitted to produce US waves and at the same time to be used for the interference antenna. The signals used for US waves are initially amplified with an ultrasonic amplifier⁵ by 13 dB. Then, the amplified signals are delivered to the US emitter through a double-shielded cable and a coaxial cable sheathed by a copper pipe. At the connection of the two cables there is a 50Ω resistance. The signals used for the interference antenna are initially adjusted in phase and amplitude and then amplified. Figure 4.4 shows a schematic diagram of the US electronics.

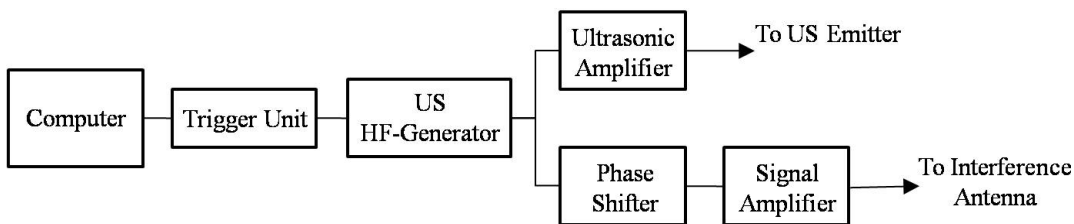


Figure 4.4: US electronics. The signals are triggered by the computer. The trigger unit is used to adjust the pulse length and delay.

4.2.1 Ultrasound Emitter

The sound emitter consists of a piezoelectric ceramic to generate US, an aluminum box to shield the high frequencies interference as much as possible, and a fused quartz rod as a sound director. The piezoelectric ceramic which receives the amplified signals through the sheathed coaxial cable is conducted by a glue to the inner side of the aluminum box (mass) with a minimum wall thickness of 2 mm. In aluminum, the skin depth is 0.019 mm at a frequency of 20 MHz [14] which is close to the frequencies used here. Inside the box, as shown in Figure 4.3, the signals go through a coil that serves as an electrical impedance matching. US is transferred through the aluminum box into the sample via a fused quartz rod. The fused quartz rod, 36 mm long and 6 mm in diameter, is attached to the aluminum box from outside just across the position of the ceramic. Both the ceramic and the quartz glass rod have the same diameter. The acoustic impedance mismatch from aluminum to quartz glass is about 15%. Values of acoustic impedances of aluminum and quartz glass are already show in Table 2.1. The US should be precisely tuned to the Larmor frequency of protons in the sample. Figure 4.5 shows the resonance frequencies of the US emitter and the NMR antenna. It can be noticed from the graph that matching of the resonance frequencies occurs at about 18.26 MHz.

⁴Marconi Instruments.

⁵Wideband RF Amplifier.

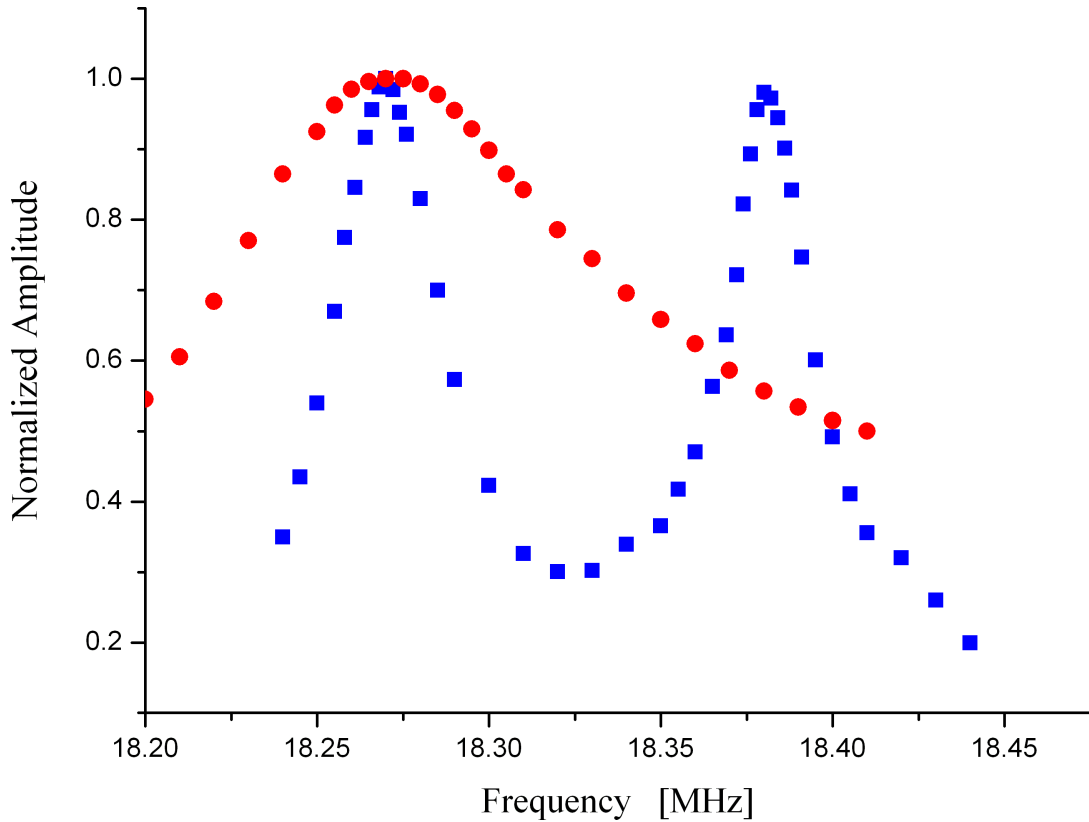


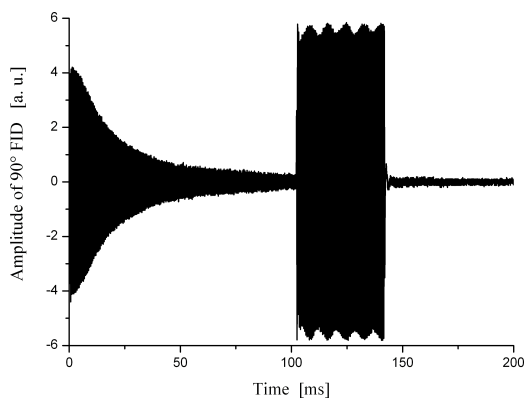
Figure 4.5: Resonance frequencies: The resonance frequency of the NMR antenna is shown in red. The resonance frequency of the US emitter is shown in blue. As seen, frequency matching occurs at about 18.26 MHz.

4.2.2 Electromagnetic Crosstalk

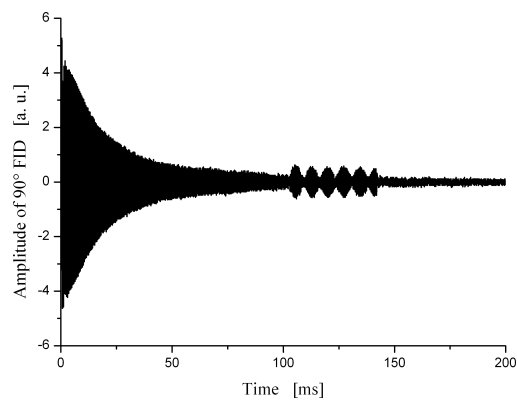
Electromagnetic crosstalk is generated when coupling resonant US with the nuclear spin system at the Larmor frequency. If the US system emits electromagnetic radiation at the operating frequency, it can be received by the NMR antenna and then amplified. This signal gains high amplitude at the amplifier in the receiving unit and it gets saturated. Therefore, an essential role in the design and operation of the US system is to prevent electromagnetic crosstalk. Thus, a shielding aluminum box is also constructed for the NMR antenna to reduce the penetration of the electromagnetic signals. Figure 4.6a shows the amplitude of electromagnetic crosstalk while the shielding box of the NMR antenna is without a cover. However, even when closing this shielding box, electromagnetic crosstalk is still caused by the RF fields that penetrate through the holes in the aluminum shielding that are used for cable or for the quartz glass rod. Therefore, an interference antenna is used to minimize this remaining crosstalk shown in Figure 4.6b. The interference antenna with an 18 pF capacitor as an impedance matching is located around the quartz glass rod. It receives the signal from the high frequency generator (see Figure 4.4). However, this signal is adjusted by phase shifters⁶ and amplitude controlled by the signal amplifier⁷ so that it minimizes the electromagnetic crosstalk by destructive interference. Figure 4.6c shows the effect of this interference antenna on reducing the electromagnetic crosstalk.

⁶NSEC Delay 2058 by Canberra

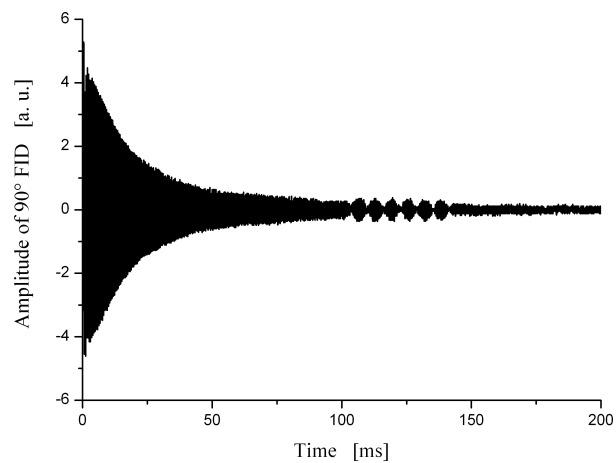
⁷Triple Power Supply EAPS 3332-03



(a) Electromagnetic crosstalk without lid on and without antenna. A 90° FID of a distilled water sample is triggered at 0 ms. US is on between 100 ms and 400 ms.



(b) Electromagnetic crosstalk with lid on but without antenna.



(c) Electromagnetic crosstalk with lid on and with antenna.

Figure 4.6: Electromagnetic crosstalk. As seen in (b) it has been reduced very much comparing to (a). And in (c) it has been reduced even further.

Chapter 5

Measurements and Results

In this chapter the measurements made during the course of this work and the obtained results are presented. The samples used for the measurements were distilled water, aqueous solutions with $1.3 \mu\text{m}$ symmetric and asymmetric magnetic particles (MPs), and 50 nm symmetric and asymmetric magnetic nanoparticles (MNPs). The volume of the samples tested in all measurements was $100 \mu\text{l}$.

5.1 Preliminary Measurement

There are several parameters that must be set before a spectrum can be recorded. The lengths of the 90° and 180° pulses were determined to be $12 \mu\text{s}$ and $24 \mu\text{s}$, respectively. Shimming the magnet was necessary to make the magnetic field more homogeneous and to obtain better spectral resolution. Also, all parts of the NMR electronics were tested and optimized. In each measurement 10 data points were recorded, and to avoid attenuation of the signal, the repetition time (TR) was set at 20 s. Figure 5.1 shows an FID of a 90° read-out pulse for a water sample obtained experimentally at the resonance frequency $\nu_0 = 18.253 \text{ MHz}$.

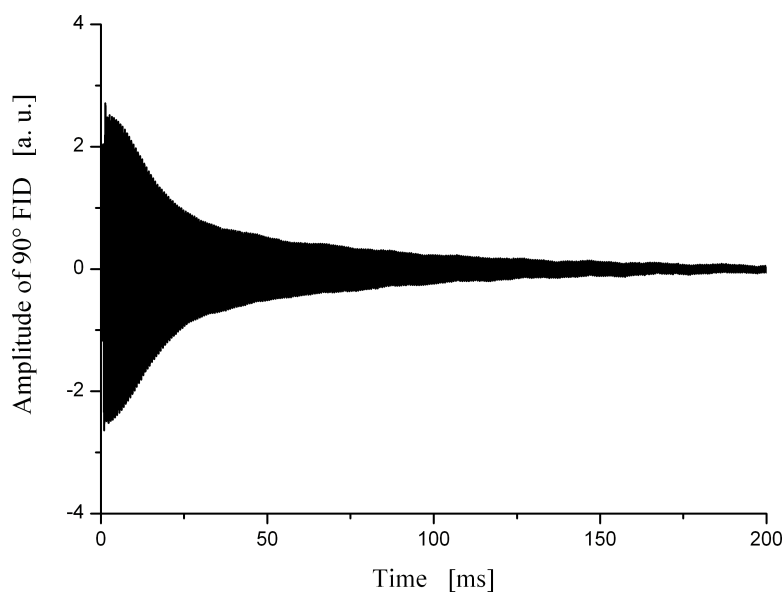


Figure 5.1: FID of 90° read-out pulse for a distilled water sample.

Figure 5.2 shows the graph of the FFT of this 90° FID. Full width at half maximum (FWHM) is determined to be $\Delta\nu_{1/2} = 14$ Hz and $T_2^* = 143 \pm 5$ ms.

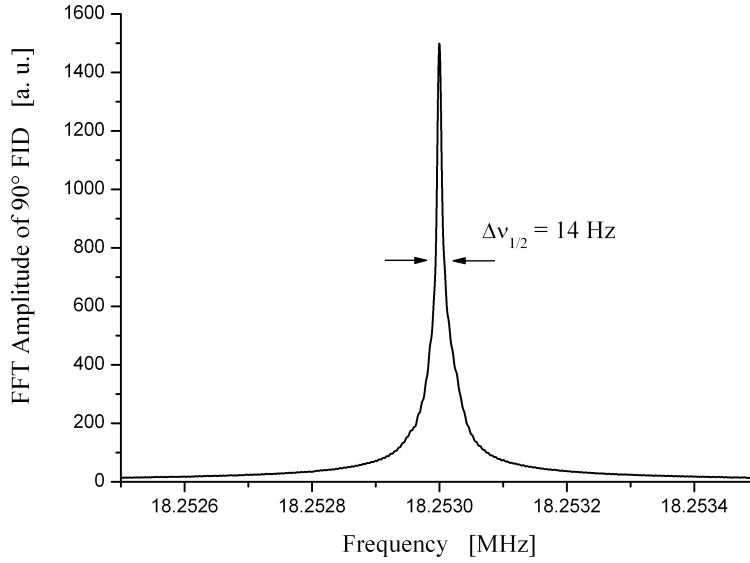


Figure 5.2: FFT Amplitude of the FID of 90° read-out pulse for a distilled water sample. $\nu_0 = 18.253$ MHz, FWHM = 14 Hz.

5.2 Measurements of T_1

5.2.1 Method

The inversion recovery sequence was used to measure the spin-lattice relaxation time T_1 . The intensity of the detected magnetization $M_z(t)$ is given by

$$M_z(t) = M_0(1 - 2 \exp(-t/T_1)) \quad (5.1)$$

$$M_z(t) = M_0(1 - 2 \exp(-R_1 t)), \quad (5.2)$$

where M_0 corresponds to the equilibrium magnetization, t is the inversion time or the time delay of the 90° pulse, and $R_1 = 1/T_1$ is the longitudinal relaxation rate. Figure 5.3 shows a simple diagram for the the recovery of the longitudinal magnetization M_z after a 180° inversion pulse. If the sample is water, then

$$R_1 = R_1^S, \quad (5.3)$$

where R_1^S is the relaxation rate due to proton-solvent interactions. However, if the sample is an aqueous solution with suspended magnetic particles, then

$$R_1 = R_1^S + R_1^M, \quad (5.4)$$

where R_1^M is the relaxation rate due proton-magnetic particles interactions for a given concentration.

T_1 is measured by equating the amplitude of the FID of the 90° read-out pulse to zero, i.e. $M_z(t)$ is set zero at $t = t_0$. After determining t_0 experimentally, T_1 is calculated by the following equation:

$$T_1 = \frac{t_0}{\ln(2)}.$$

The values of t_0 and T_1 for distilled water were found to be:

$$\begin{aligned} t_0 &= 1580 \pm 10 \text{ ms} \\ T_1 &= 2279 \pm 14 \text{ ms}. \end{aligned}$$

Values of T_1 for other samples will be presented later.

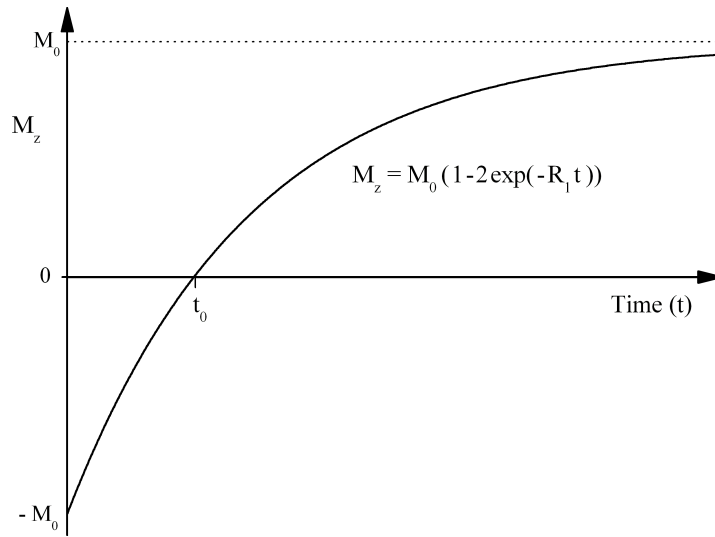


Figure 5.3: Recovery of the longitudinal magnetization M_z after a 180° pulse inversion. At t_0 the amplitude of the 90° pulse FID is equal to zero.

5.2.2 Application of Ultrasound

The inversion recovery experiment was employed in the presence of a resonant US wave to measure the modified longitudinal relaxation time of different samples. The sequence was constructed as shown in Figure 5.4. The resonant US was applied to the samples between the 180° and 90° pulses, and the 90° FID was recorded. The delay time of the 90° pulse was shorter than t_0 of the sample. In equation (5.6) R_1 can be regarded as a sum of rates of different relaxation mechanisms. For a water sample:

$$R_1 = R_1^S + R_1^{US}. \quad (5.5)$$

For a sample of an aqueous solution with suspended magnetic particles:

$$R_1 = R_1^S + R_1^M + R_1^{US}. \quad (5.6)$$

R_1^{US} is the assumed supplementary contribution of US to the total relaxation rate R_1 .

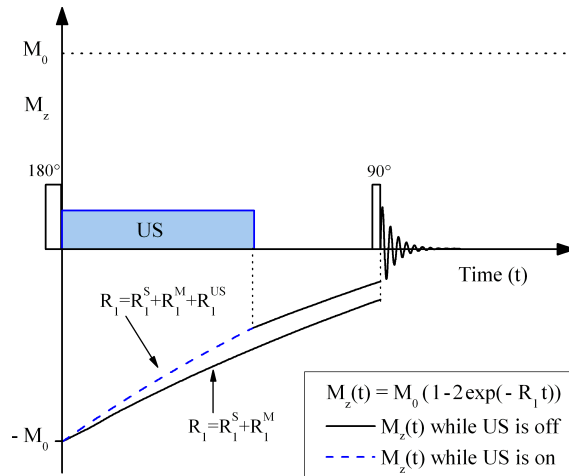


Figure 5.4: A diagram of the inversion recovery sequence with the application of US. The 90° pulse FID is recorded before the value of t_0 of the sample. When US is switched off, the proton-solvent interactions R_1^S and the proton-magnetic particles interactions R_1^M contribute to the relaxation rate R_1 . When US is on, an additional contribution R_1^{US} is added.

5.3 Results

Figure 5.5 shows the read-out of the complete inversion recovery sequence. The US pulse is triggered at 0 ms with a pulse length of 400 ms. The delay time of the 90° pulse is 550 ms. The FID signals were recorded before t_0 of the sample and within a time window of 300 ms that immediately followed the 90° read-out pulse. The presented results are for the FFT amplitudes of the 90° read-out pulse FID.

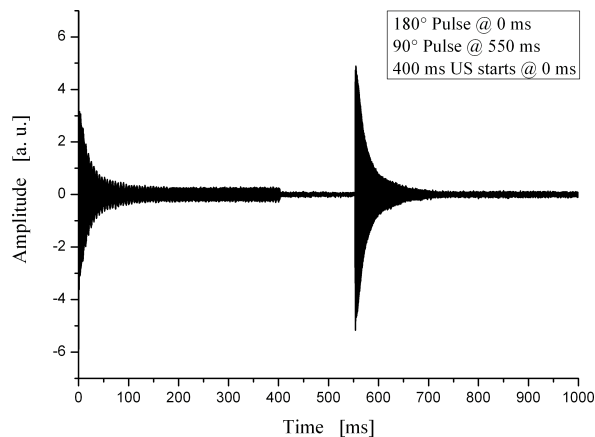


Figure 5.5: Experimental read-out of the complete inversion recovery sequence with the application of US. 180° pulse is triggered at 0 ms, 90° pulse is triggered at 550 ms, and US is triggered at 0 ms with a pulse length 400 ms.

During measurements the electromagnetic crosstalk was reduced to minimum as stated earlier by adjusting the interference antenna in phase and amplitude. To assure the stability of the frequency of the spectrometer, the Helmholtz coils were turned on. The frequency of US was matched to the Larmor frequency, and its value will be mentioned in each result.

For comparison, data of the FID signals were collected when US is switched on and off, successively. The presented results of the FFT amplitudes are averages of some read-out data points. These averaged data points are connected by B-Spline for eye-guide.

5.3.1 Water Sample

The first measurement to investigate the effect of US on the relaxation rate was performed on a water sample. Figure 5.6 shows the FFT amplitudes of the 90° pulse FID in the inversion recovery sequence with and without US. In the setup the Larmor frequency was $\nu_0 = 18.253$ MHz. During this measurement the US frequency ν_{US} was fixed at 18.253 MHz matching the Larmor frequency, and the US amplitude was 1 dBm. The FFT amplitude of the 90° FID is shown in red when US is switched off, and in blue when US is on. The difference of these two amplitudes is plotted in green. No effect is observed within the experimental error.

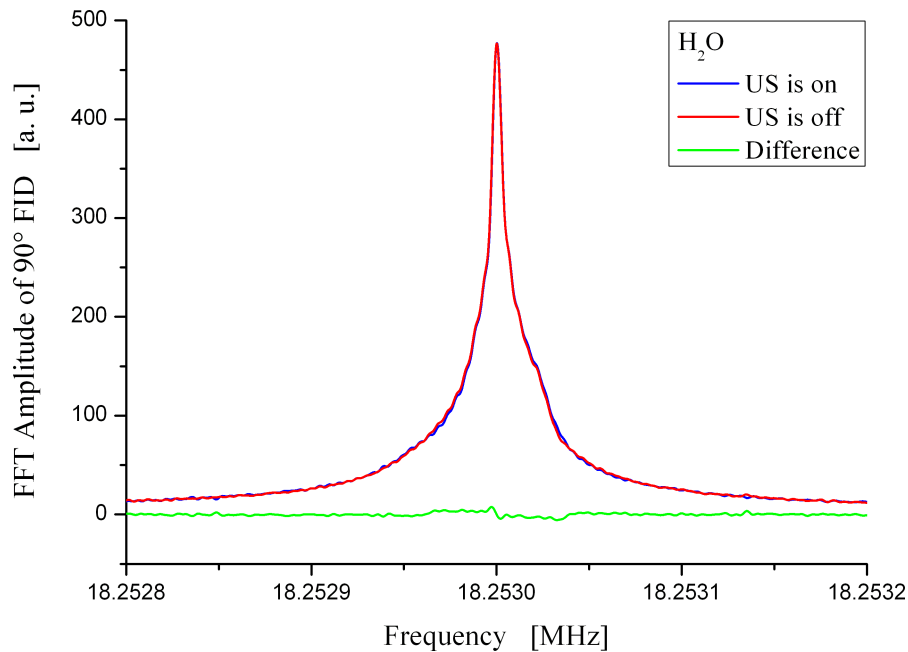


Figure 5.6: The FFT amplitudes of the 90° pulse FID for a sample of distilled water. When US is off, the amplitude is shown in red. When US is on, the amplitude is shown in blue. The difference between these two amplitudes is plotted in green. The US frequency ν_{US} matched the Larmor frequency ν_0 at 18.253 MHz.

5.3.2 Sample of Aqueous Solution with 1.3 μm Magnetic Particles

Values of T_2^* and T_1 of some dilutions of the aqueous solutions with suspended 1.3 μm MPs are presented in Table 5.1. T_2^* was calculated from the 90° FID sequence. t_0 was measured while US was switched off.

Dilution	Concentration [mg/ml]	$T_2^* \pm 5$ [ms]	$t_0 \pm 10$ [ms]	$T_1 \pm 14$ [ms]
1	1.62×10^{-2}	49	1070	1544
2	9.72×10^{-3}	53	1150	1659
3	6.08×10^{-3}	-	1360	1962
4	1.62×10^{-3}	-	1480	2135
5	1.62×10^{-3}	80	1400	2020

Table 5.1: Values of T_2^* and T_1 of some dilutions of the aqueous solutions with suspended 1.3 μm MPs.

The first four dilutions are solvents with suspended symmetric MPs. Dilution 5 was a solvent with suspended AsMPs. Dilution 1 was used for the preparation of AsMPs. The effect of US on the relaxation rate was investigated for dilutions 4 and 5 for comparison because their T_1 values are close.

Figure 5.7 shows the FFT amplitudes of the 90° FID with and without US for dilution 4 of symmetric 1.3 μm MPs. The difference between the amplitudes is plotted in green. No effect is observed within the experimental error. The US frequency was at 18.277 MHz, and the US amplitude was 1 dBm.

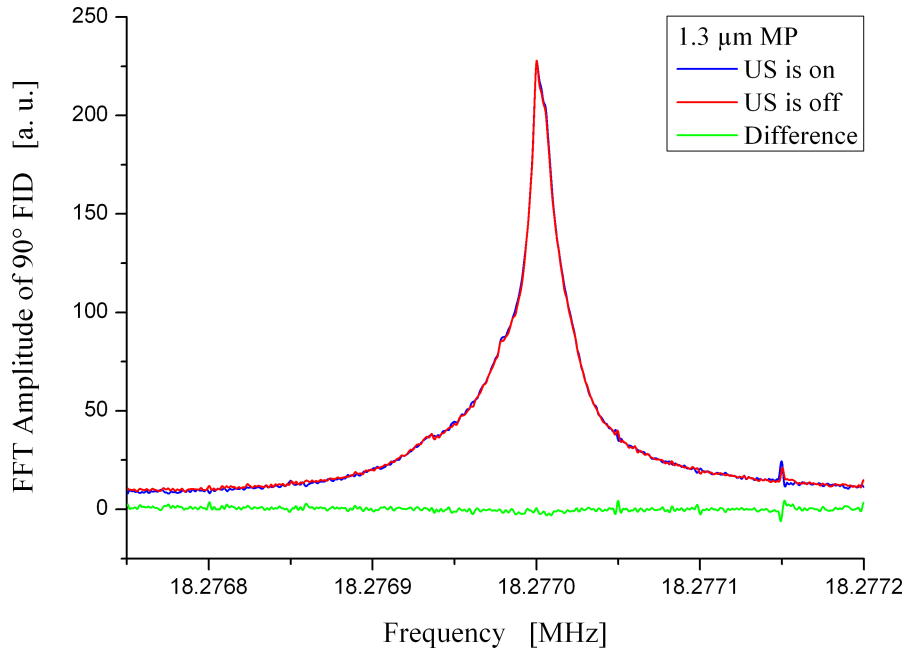


Figure 5.7: The FFT amplitudes of the 90° pulse FID for a sample of an aqueous solution with 1.3 μm MPs. The US frequency ν_{US} matched the Larmor frequency ν_0 at 18.277 MHz.

Figure 5.8 shows the FFT amplitudes of the 90° FID with and without US for dilution 5 of 1.3 μm AsMPs. The difference between the amplitudes which is plotted in green shows a

small peak at the resonance frequency. A decrease in the FFT amplitude of the 90° FID is observed. The US frequency ($\nu_{US} = 18.277$ MHz) and amplitude (1 dBm) were the same as used for the solvent of symmetric $1.3 \mu\text{m}$ MPs. The percentage difference relative to the amplitude with US turned off is plotted in Figure 5.9. Maximum percentage difference that is observed when $\nu_0 = \nu_{US}$ is about 7 % .

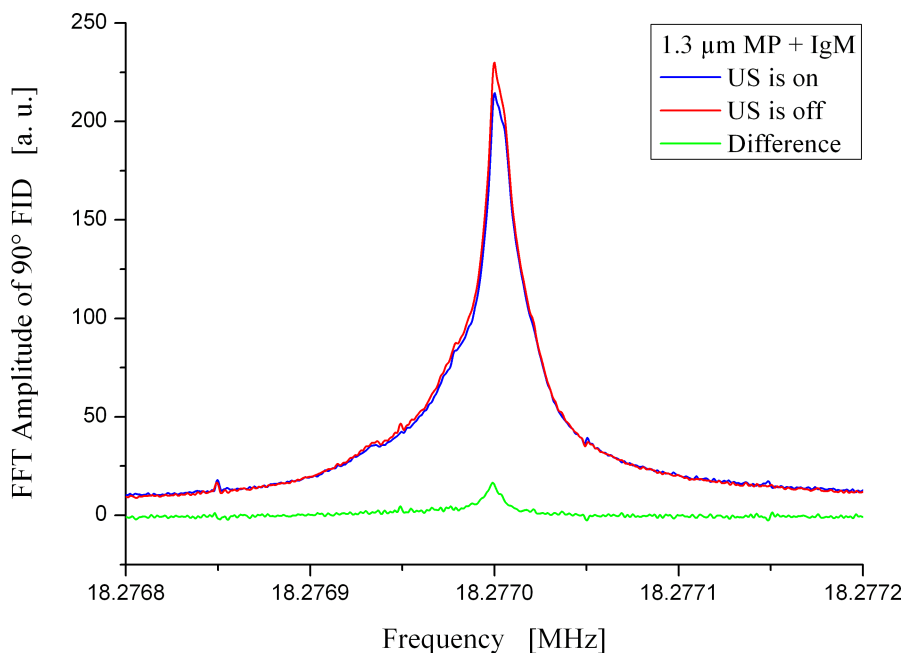


Figure 5.8: The FFT amplitudes of the 90° pulse FID for a sample of an aqueous solution with $1.3 \mu\text{m}$ MPs with the IgM antibody attached. The US frequency ν_{US} matched the Larmor frequency ν_0 at 18.277 MHz.

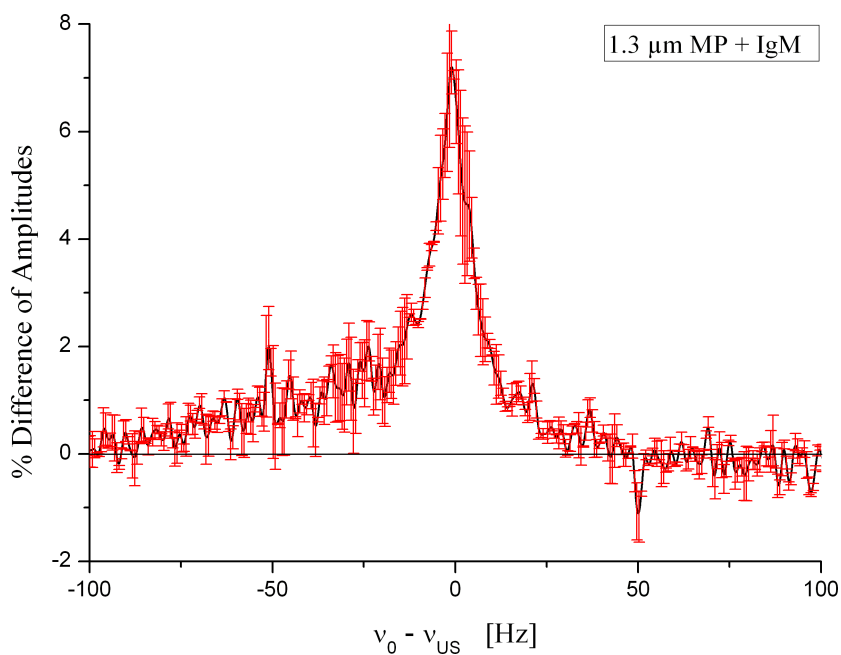


Figure 5.9: The relative percentage difference is plotted against the frequency difference between ν_0 and ν_{US} . An increase in the percentage difference is observed when $\nu_0 = \nu_{US}$.

5.3.3 Sample of Aqueous Solution with 50 nm Magnetic Nanoparticles

Values of T_2^* and T_1 of some dilutions of the aqueous solutions with suspended 50 nm MNPs are presented in Table 5.2.

Dilution	Concentration [mg/ml]	$T_2^* \pm 5$ [ms]	$t_0 \pm 10$ [ms]	$T_1 \pm 14$ [ms]
1	1.28×10^{-3}	111	310	447
2	3.66×10^{-4}	-	550	793
3	1.83×10^{-4}	105	920	1327
4	1.83×10^{-4}	105	950	1370

Table 5.2: Values of T_2^* and T_1 of some dilutions of the aqueous solutions with suspended 50 nm MNPs.

The first three dilutions are solvents with suspended symmetric MNPs. Dilution 4 was a solvent with suspended AsMPs. The effect of US on the relaxation rate was investigated for dilutions 4 and 5 for comparison because their T_1 values are close.

Figure 5.10 shows the FFT amplitudes of the 90° FID with and without US for dilution 4 of symmetric 50 nm MNPs. The difference between the amplitudes is plotted in green. No effect is observed within the experimental error. The US frequency was at 18.253 MHz, and the US amplitude was 1 dBm.

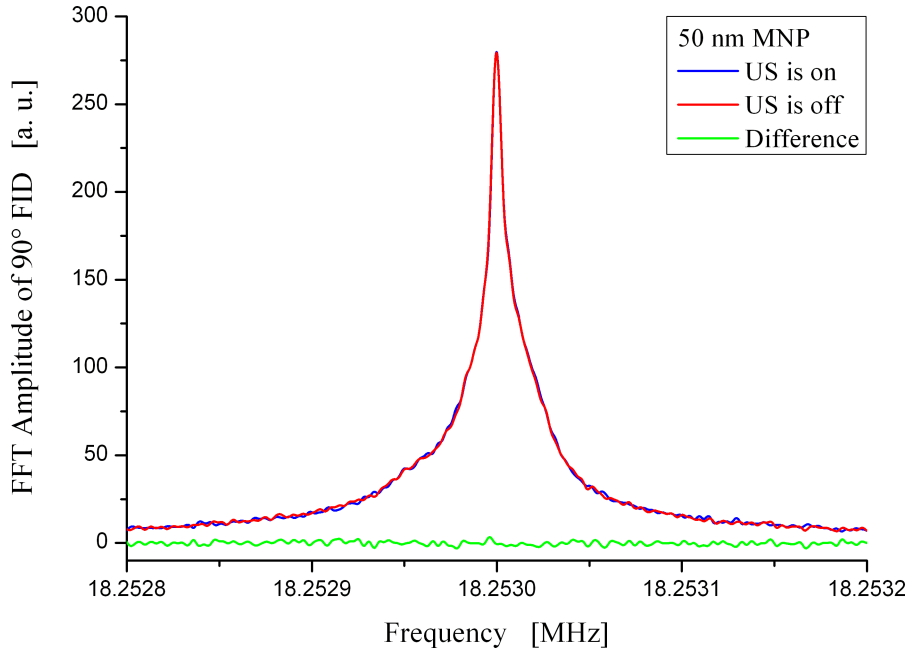


Figure 5.10: The FFT amplitudes of the 90° pulse FID for a sample of an aqueous solution with 50 nm MNPs. The US frequency ν_{US} matched the Larmor frequency ν_0 at 18.253 MHz.

Figure 5.11 shows the FFT amplitudes of the 90° FID with and without US for dilution 4 of 50 nm AsMPs. The difference between the amplitudes which is plotted in green shows a large peak at the resonance frequency. A significant decrease in the FFT amplitude of the 90° FID is observed. The US frequency ($\nu_{US} = 18.253$ MHz) and amplitude

(1 dBm) were the same as used for the solvent of symmetric 50 nm MNPs. The percentage difference relative to the amplitude with US turned off is plotted in Figure 5.12. Maximum percentage difference that is observed when $\nu_0 = \nu_{US}$ is about 30 %.

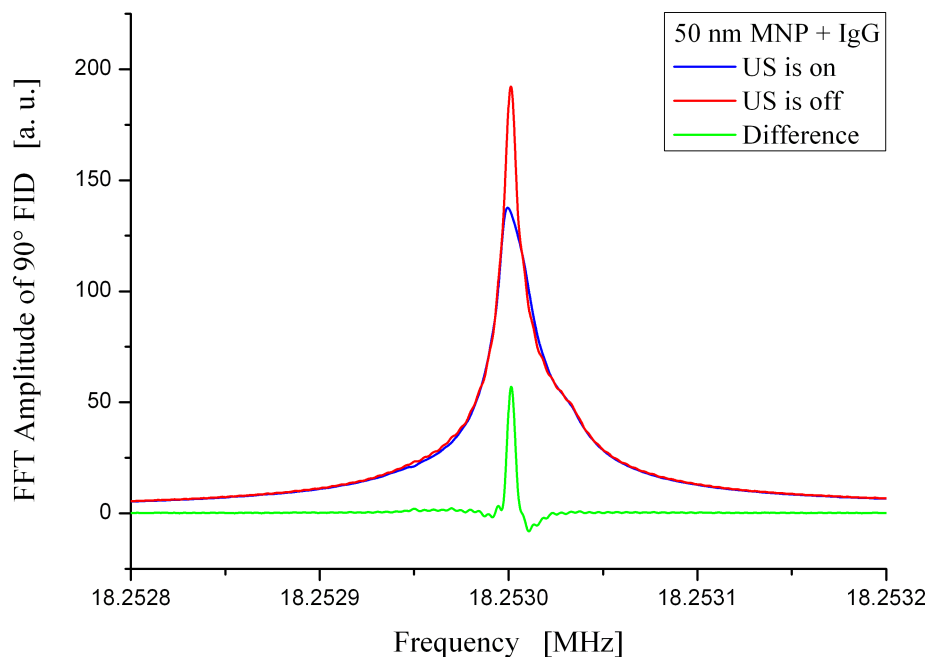


Figure 5.11: The FFT amplitudes of the 90° pulse FID for a sample of an aqueous solution with 50 nm MNPs with the IgG antibody attached. The US frequency ν_{US} matched the Larmor frequency ν_0 at 18.253 MHz.

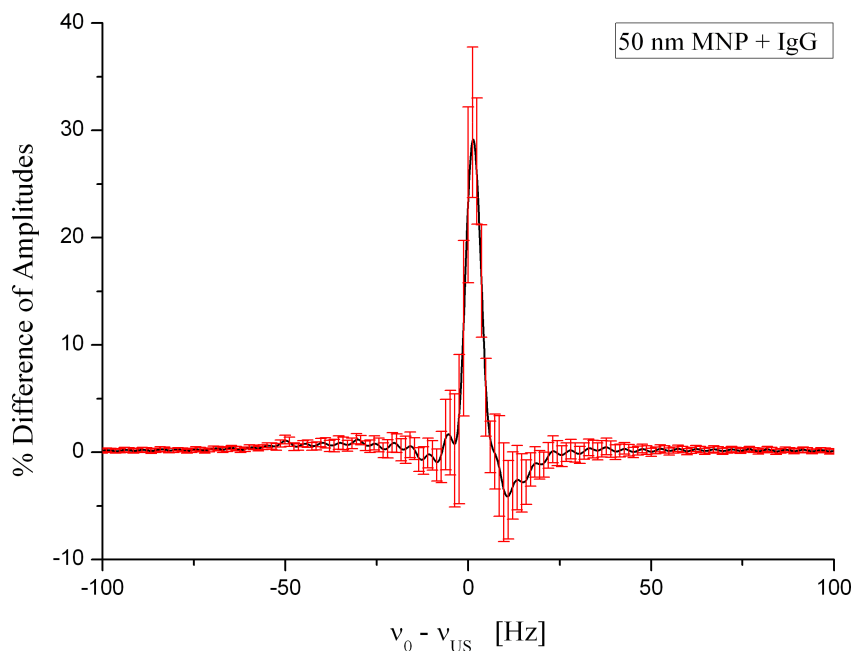


Figure 5.12: The relative percentage difference is plotted against the frequency difference between ν_0 and ν_{US} . An significant increase in the percentage difference is observed when $\nu_0 = \nu_{US}$.

Chapter 6

Discussion

The observed coupling of US to the nuclear spin system through the introduction of asymmetric magnetic nanoparticles is shown by the decrease of the FFT amplitude of the measured 90° FID. It is worth mentioning again that the 90° read-out pulse is applied at an inversion time $t_{90} = 550$ ms before the t_0 of the sample. The measured value of t_0 for distilled water is 1580 ms, for the sample of the aqueous solution containing $1.3 \mu\text{m}$ MPs it is 1400 ms, and for the sample containing 50 nm MNPs it is 950 ms. The supplementary contribution of US R_1^{US} to the total relaxation rate R_1 is observed as a resulting decrease in the FFT amplitude because the 90° FID is recorded before the time t_0 . A schematic diagram of the inversion recovery sequence that was used for measurements is shown in Figure 5.4.

To verify that this influence of US on the spectral FID amplitude is not due to any remaining leakage of electromagnetic crosstalk, a sample of distilled water and samples of aqueous solutions with symmetrical magnetic particles were examined. The absence of the US effect in these samples subjected to the same experimental conditions confirms the negligibility of the electromagnetic crosstalk. Graphs of these samples are already shown in Chapter 5. These unobservable changes in the spectral FID amplitudes are in accordance with results presented by Bowen [10]. Furthermore, US-induced effects, such as cavitation, temperature changes, or coherent motion of particles, possibly influencing the spin-lattice relaxation time, can be neglected here.

In the preparation of asymmetrical magnetic particles the particles are initially sedimented using a combination of a centrifugal force and a magnetic force. Because $1.3 \mu\text{m}$ MPs are big enough to be seen under the microscope in our laboratory, they were used to ensure the sedimentation process was successful. In addition to this optical control, a T_1 test was performed. After the sedimentation process and before adding the antibody, T_1 for a sample of the aqueous solution (without disturbing the bottom surface) was measured to be 2308 ± 14 ms. This value was very close to the value of T_1 for a water sample measured on the same day. Table 6.1 shows a comparison of the values of T_1 for a sample of the aqueous solution containing $1.3 \mu\text{m}$ MPs before and after sedimentation process and a water sample.

Sample	$T_1 \pm 14$ [ms]
Solution before sedimentation	1544
Solution after sedimentation	2308
Distilled water	2330

Table 6.1: Comparison between T_1 values for samples of aqueous solution of $1.3 \mu\text{m}$ MPs before and after the sedimentation process and a water sample measured on the same day, i.e under the same experimental conditions.

However, the sedimented 50 nm MNPs were too small to be clearly seen by the microscope. Therefore, only a T_1 test was performed for a sample of the aqueous solution after the sedimentation process. T_1 for this aqueous solution was measured to be 2193 ± 14 ms which was very close to the value of T_1 for a water sample measured on the same day. Table 6.2 shows a comparison of the values of T_1 for a sample of the aqueous solution containing 50 nm MNPs before and after sedimentation process and a water sample.

Sample	$T_1 \pm 14$ [ms]
Solution before sedimentation	1544
Solution after sedimentation	2193
Distilled water	2279

Table 6.2: Comparison between T_1 values for samples of aqueous solution of 50 nm MNPs before and after the sedimentation process and a water sample measured on the same day, i.e under the same experimental conditions.

According to the values of T_1 presented in the above tables, the sedimentation of the particles was successfully achieved. The values of T_1 for the aqueous solutions before and after sedimentation are obviously distinct. It is clear that it is resulting from the fact that the particles are fixed to the bottom surface as a monolayer. Consequently, the antibody could be from one side only attached to the magnetic particles and asymmetry was fulfilled.

The spectral FID amplitudes for the aqueous solutions containing AsMNPs were decreased if the ν_{US} matched ν_0 . A pronounced change in the FID's lineshape is observed when this resonance condition was fulfilled. For the aqueous solution containing 50 nm MNPs with the IgG antibody attached, the lineshape of the relative signal loss has a full width at half maximum of approximately the bandwidth of the US pulse ($1/t_{US} = 2.5$ Hz). This strongly supports the interpretation of the findings presented in Chapter 3 as a nuclear magnetic acoustic resonance phenomenon. Therefore, the US-induced motion of AsMNPs indeed generated RF waves at ν_{US} , which stimulated transitions of the proton nuclear magnetic moments between their Zeeman energy states.

It is important to note that these results are reproducible. Figure 6.1 shows the first results obtained for a sample of aqueous solution containing 50 nm MNPs. These MNPs were ordered several months before the ones used for the results presented in Chapter 5. According to the particles technical data sheet from the manufacturer, these particles can be stored for three months. Therefore, new MNPs were ordered to perform extra measurements on them. Figure 6.2 shows a comparison between the results of the percentage difference in the FFT amplitudes obtained using two different orders of 50 nm

MNPs. Although these measurements were not taken at exactly the same US amplitude, their results are comparable. Therefore, the results observed for the decrease of the FFT amplitude when US is applied are reproducible for aqueous solutions with 50 nm MNPs with the IgG antibody attached.

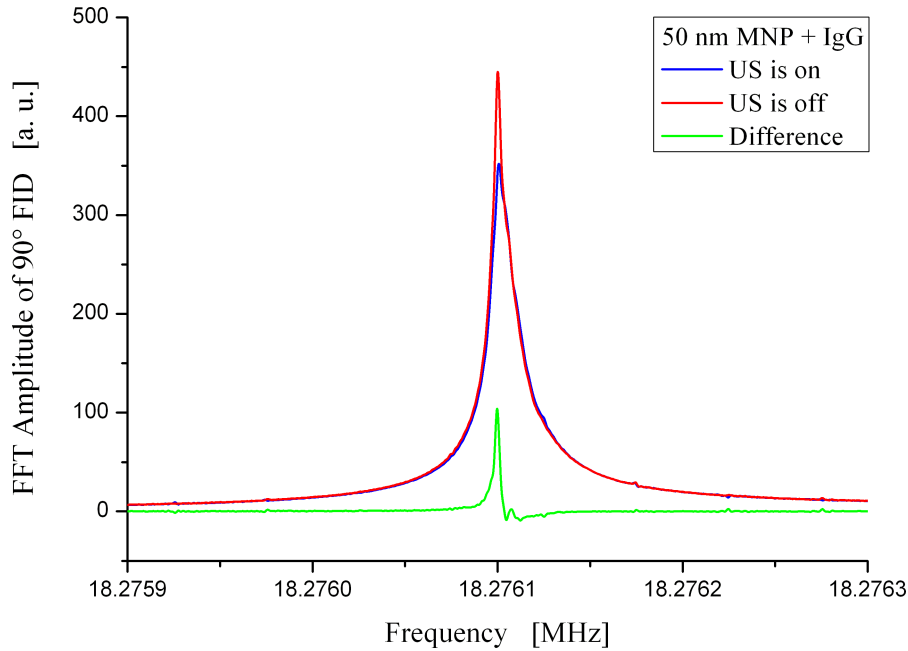


Figure 6.1: Early measurements on 50 nm MNPs. The FFT amplitudes of the 90° pulse FID for a sample of an aqueous solution with 50 nm MNPs with the IgG antibody attached. The US frequency ν_{US} matched the Larmor frequency ν_0 at 18.2761 MHz.

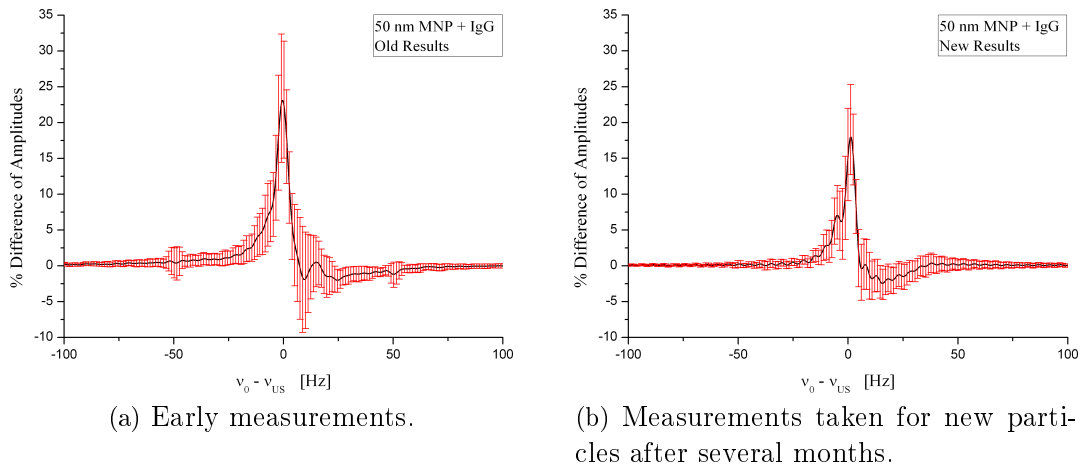


Figure 6.2: A comparison between the results of the percentage difference in the FFT amplitudes obtained using two different orders of 50 nm MNPs. The relative percentage difference is plotted against the frequency difference between ν_0 and ν_{US} . A pronounced change in the FID's lineshape caused by the application of US is reproducible when using AsMNPs. The increase in the percentage difference is observed when $\nu_0 = \nu_{US}$.

Further measurements were carried out using $1.3 \mu\text{m}$ AsMPs and 50 nm AsMNPs with the variation of the US amplitude. Figure 6.3 shows the results obtained for samples of aqueous solutions containing $1.3 \mu\text{m}$ MPs with the IgM antibody attached. The percentage difference of FFT amplitudes of the 90° read-out FIDs are plotted against the different values of the US amplitude.

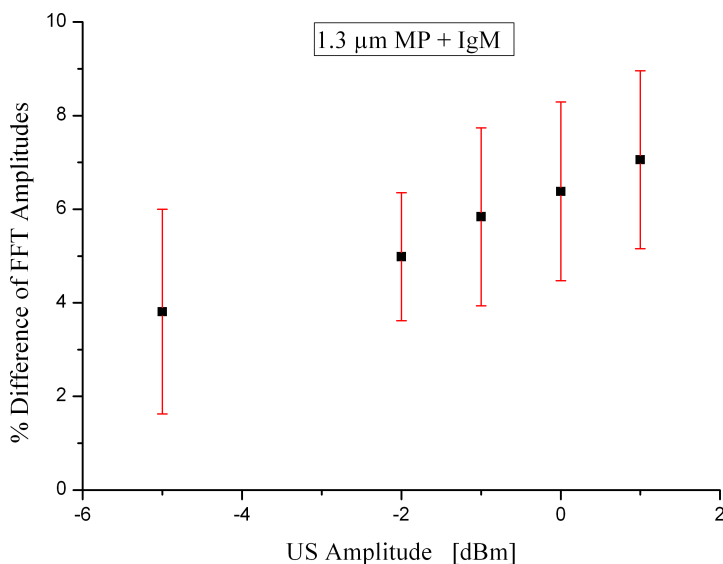


Figure 6.3: The percentage difference of FFT amplitudes of the 90° pulse FID versus the US amplitude for a sample of an aqueous solution with $1.3 \mu\text{m}$ MPs with the IgM antibody attached.

The results obtained for samples of aqueous solutions containing 50 nm MNPs with the IgG antibody attached are shown in Figure 6.4. The percentage difference of the FFT amplitudes of the 90° read-out FIDs are plotted against the different values of the US amplitude. Graphs of the FFT amplitudes of the 90° FID with and without US for different US amplitudes are presented in Appendix C.

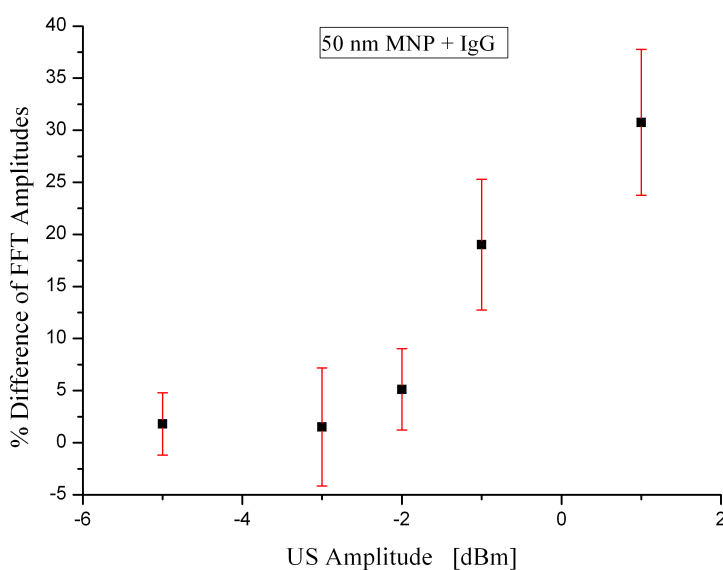


Figure 6.4: The percentage difference of FFT amplitudes of the 90° pulse FID versus the US amplitude for a sample of an aqueous solution with 50 nm MNPs with the IgG antibody attached.

It can be seen from both graphs that the relative signal loss increases with the increase of the US amplitude. By comparison of the results in both graphs, it is observed that the US effect is greater when using aqueous solutions of 50 nm MNPs with 150 kDa IgG antibody attached than when using aqueous solutions of 1.3 μm MPs with 900 kDa IgM antibody attached. This behavior is quite reasonable because of the difference in sizes of AsMNPs. The ultrasonic wave has a wavelength ($\lambda_{US} = 81 \mu\text{m}$) that is 10^3 times greater than the 50 nm MNP diameter while only 60 times greater than the 1.3 μm MP diameter. The smaller particles are expected to be accelerated faster by the movement of the surrounding medium causing the release of more RF waves to the near field region of the particle. Thus, a bigger effect is observed for the aqueous solutions of 50 nm MNPs with the IgG antibody attached specially at higher amplitude.

The corresponding values of US power to the values of the US amplitude were measured recently. Table 6.3 shows the measured values of US power with respect to the US amplitude used in the measurements.

US Amplitude [dBm]	US Power [W/cm^2]
-5	0.8 ± 0.4
-3	1.4 ± 0.6
-2	1.8 ± 0.8
-1	2 ± 1
1	3 ± 1

Table 6.3: Measured values of US power corresponding to the experimental values of US amplitude.

The US effect on the signal loss was investigated with the variation of US pulse length. It was observed that the relative signal loss increases with the increase of the US pulse length. Figure 6.5 shows the results obtained for samples of aqueous solutions containing 50 nm MNPs with the IgG antibody attached. The percentage difference of FFT amplitudes of the 90° read-out FIDs are plotted against different values of the US pulse length.

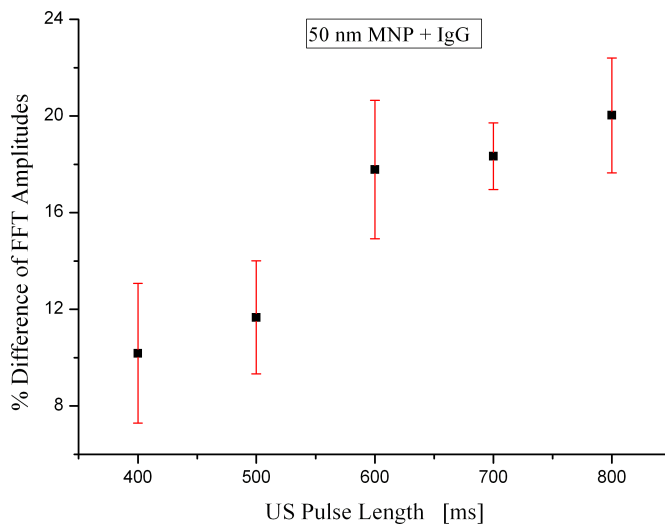


Figure 6.5: The percentage difference of the FFT amplitudes of the 90° pulse FID versus the US pulse length for a sample of an aqueous solution with 50 nm MNPs with the IgG antibody attached.

The measurements shown in the graph are obtained for an US amplitude of 1 dBm. In the graph the relative signal loss at 400 ms US is about 10 % which is much lower than what was shown earlier 30 %. One possible reason for this decrease is that these measurements were taken after three months from the purchase date of the MNPs. It was mentioned earlier that the technical data sheet states that storage time of the MNPs is three months. This means that the MNPs are not as effective as when they have not passed the validation date. Therefore, all other values at higher US pulse lengths are less than their actual values, but they can be used to see the behavior of the effect when increasing the US pulse length.

A rough calculation for the effect of US on the longitudinal relaxation rate R_1 can be presented as follows. In Chapter 5, R_1 of an aqueous solution with suspended magnetic particles when US applied was given by equation (5.6) as

$$R_1 = R_1^S + R_1^M + R_1^{US}$$

R_1^S is the relaxation rate due to proton-solvent interactions, R_1^M is the relaxation rate due proton-magnetic particles interactions for a given concentration, R_1^{US} is the assumed supplementary contribution added by US.

Substituting this relaxation rate in the magnetization $M_z(t)$ equation describing in the inversion recovery experiment that was used in this work, we get

$$M_z(t_{90}) = M_0 [1 - 2 \exp(-(R_1^S + R_1^M)t_{90})] \quad (6.1)$$

$$M_z^{US}(t_{90}) = M_0 [1 - 2 \exp(-(R_1^S + R_1^M)t_{90} - R_1^{US}t_{US})] , \quad (6.2)$$

where $M_z^{US}(t_{90})$ is the magnetization when US is applied, $t_{90} = 550$ ms is the inversion time, $t_{US} = 400$ ms is the US pulse length, $R_1^S + R_1^M = 0.73 \pm 0.01$ s⁻¹ calculated from Table 5.2. By solving equations (6.1) and (6.2) using the data obtained for the FFT amplitudes of the 90° FIDs with and without US at 3 W/cm² for the aqueous solution of 50 nm MNPs with the IgG antibody attached, we get a rough estimate for the supplementary contribution added by US:

$$R_1^{US} = 0.20 \pm 0.05 \text{ s}^{-1}. \quad (6.3)$$

Thus,

$$R_1 = R_1^S + R_1^M + R_1^{US} = 0.93 \pm 0.05 \text{ s}^{-1}. \quad (6.4)$$

Therefore, the supplementary contribution added by US leads to an increase of the relaxation rate by about 21.5 %.

Chapter 7

Summary and Outlook

7.1 Summary

A resonant coupling mechanism has been introduced between an ultrasonic wave and the nuclear spin system in liquid samples which is mediated by mechanical properties of specially prepared magnetic nanoparticles. These particles (AsMNPs) were prepared by chemically attaching streptavidin coated magnetic nanoparticles with biotinylated antibody molecules from one side only. Before attachment, they were sedimented by a combination of a centrifugal force and a magnetic force. Two sizes of magnetic particles were used for measurements. $1.3 \mu\text{m}$ magnetic particles (MPs) were attached with the IgM antibody molecules, and the corresponding concentration of MPs in the solvent was 1.62×10^{-3} mg/ml. 50 nm magnetic nanoparticles (MNPs) were attached with IgG antibody molecules, and the corresponding concentration of MNPs in the solvent was 1.83×10^{-4} mg/ml.

The inversion recovery experiment was employed in the presence of a resonant US wave to measure the modified longitudinal relaxation time of different samples. Samples of distilled water and aqueous solutions of symmetric and asymmetric magnetic particles were subjected to a longitudinal ultrasonic wave having a wavelength of about $80 \mu\text{m}$. US was transferred through an aluminum box into the sample via a fused quartz rod. The electromagnetic crosstalk was controlled by screening the NMR antenna and US electronics with aluminum boxes and also by using a destructive interference antenna. In the inversion recovery sequence, the resonant US was applied to the samples between the 180° and 90° pulses, and the 90° free induction decay (FID) was recorded at a time before the t_0 of the sample. The amplitudes of the fast Fourier transform (FFT) of the 90° read-out pulse FIDs were analyzed for the samples.

No changes of the FFT amplitudes with and without US were observed for samples of distilled water and aqueous solutions of symmetric MNPs. However, a decrease in the FFT amplitudes with US applied was observed for the aqueous solutions of AsMNPs. A decrease of about 7 % was observed for aqueous solutions of $1.3 \mu\text{m}$ MPs with the IgM antibody attached at an US frequency 18.277 MHz, and a significant decrease of about 30 % was observed for aqueous solutions of 50 nm MNPs with the the IgG antibody attached at an US frequency 18.253 MHz and at an US power 3 W/cm^2 . This US effect was particularly observed when the US frequency ν_{US} matched the proton Larmor frequency of the solvent ν_0 .

This US effect was also investigated for different values of US power for both kinds of AsMNPs. It was shown that the relative signal loss increased with the increase of US power. The relative signal loss was bigger for aqueous solutions of 50 nm MNPs with the IgG antibody attached due to a faster mobility of smaller particles in a liquid medium subjected to an US wave. Also, it was observed that the relative signal loss increased with the US pulse length.

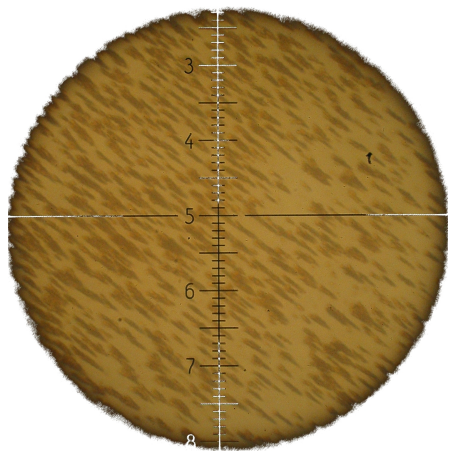
Therefore, this decrease in the FFT amplitude of the 90° FID leads to a shortening the longitudinal relaxation time T_1 of an aqueous solution with AsMNPs. The tilting behavior of AsMNPs can be regarded as a possible source for US-induced radio frequency waves. It has been experimentally shown that a new coupling mechanism between resonant US and the nuclear spin system for an aqueous solution can be achieved by this method.

7.2 Outlook

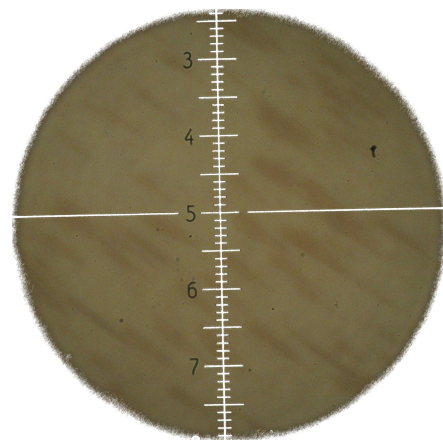
This technique promises the widespread applications of US-induced relaxation rate enhancement for characterizing non-homogeneous samples in physics, chemistry, biology, or in the material science. Also, the change in the relaxation time T_1 due to US application leads to additional information in MRI pictures. The applicable US at the NMR frequency is compatible with standard open low field MRI systems. Mobility of contrast agents and tissue can be visualized. In addition, biochemical reactions with contrast agents (molecular imaging) can be detected in a more sensitive way. It is interesting to control their effect on MRI by additional parameters, which can be switched on and off externally and depend on the properties of the surrounding tissue.

Appendix A

Microscopic Pictures

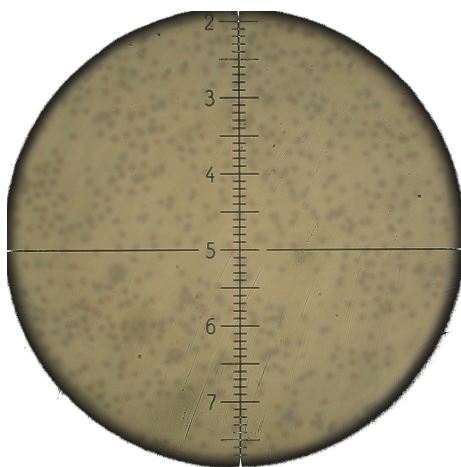


(a) Magnification: 200X

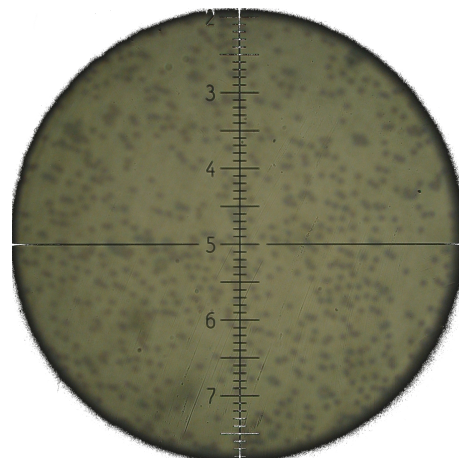


(b) Magnification: 500X

Figure A.1: Sedimentation of $1.3 \mu\text{m}$ MPs using only a rare-earth magnet. Pictures show the formation of needles.



(a) Magnification: 500X



(b) Magnification: 500X

Figure A.2: Sedimentation of $1.3 \mu\text{m}$ MPs using centrifugal force and magnetic force.

Appendix B

Particles Technical Data

Technical Data of 50 nm Magnetic Nanoparticles

Product size	50 nm
Surface	streptavidin
Quantity	1 ml
Solid quantity	2.5 mg/ml
Polydispersity index	< 0.2
Shape	cluster-typed
Density	1.4 g/ccm
Magnetization	24 emu/g particles (H = 1000 Oe)
Saturation magnetization	> 34 emu/g particles (H > 10.000 Oe)
Stable in	aqueous buffers pH > 4
Not stable in	organic solvents, acidic solutions pH < 4
Product form	suspension in PBS buffer (pH = 7.4), stabilized in 0.02 % sodium azide
Particles per ml	2.8×10^{13}
Particles per mg	1.1×10^{13}
Protein binding capacity	1.5 μ g streptavidin / mg particle
Additional remarks	Storage at 2 – 8°C for 3 months

Table B.1: Technical Data of 50 nm MNPs.

Technical Data of 1.3 μm Magnetic Particles

Product size	1.3 μm
Surface	avidin
Quantity	10 ml
Solid quantity	5 mg/ml
Polydispersity index	< 0.2
Shape	cluster-typed
Density	1.58 g/ccm
Magnetization	43 emu/g particles (H = 1000 Oe)
Saturation magnetization	> 67 emu/g particles (H > 10.000 Oe)
Stable in	aqueous buffers pH > 4
Not stable in	organic solvents, acidic solutions pH < 4
Product form	suspension in PBS buffer (pH = 7.4), stabilized in 0.02 % sodium azide
Particles per ml	2.68×10^9
Particles per mg	5.36×10^8
Protein binding capacity	0.76 nmole of Biotin-FITC / mg particle
Additional remarks	Storage at 2 – 8°C for 3 months

Table B.2: Technical Data of 1.3 μm MPs.

Appendix C

Graphs of FFT Amplitudes

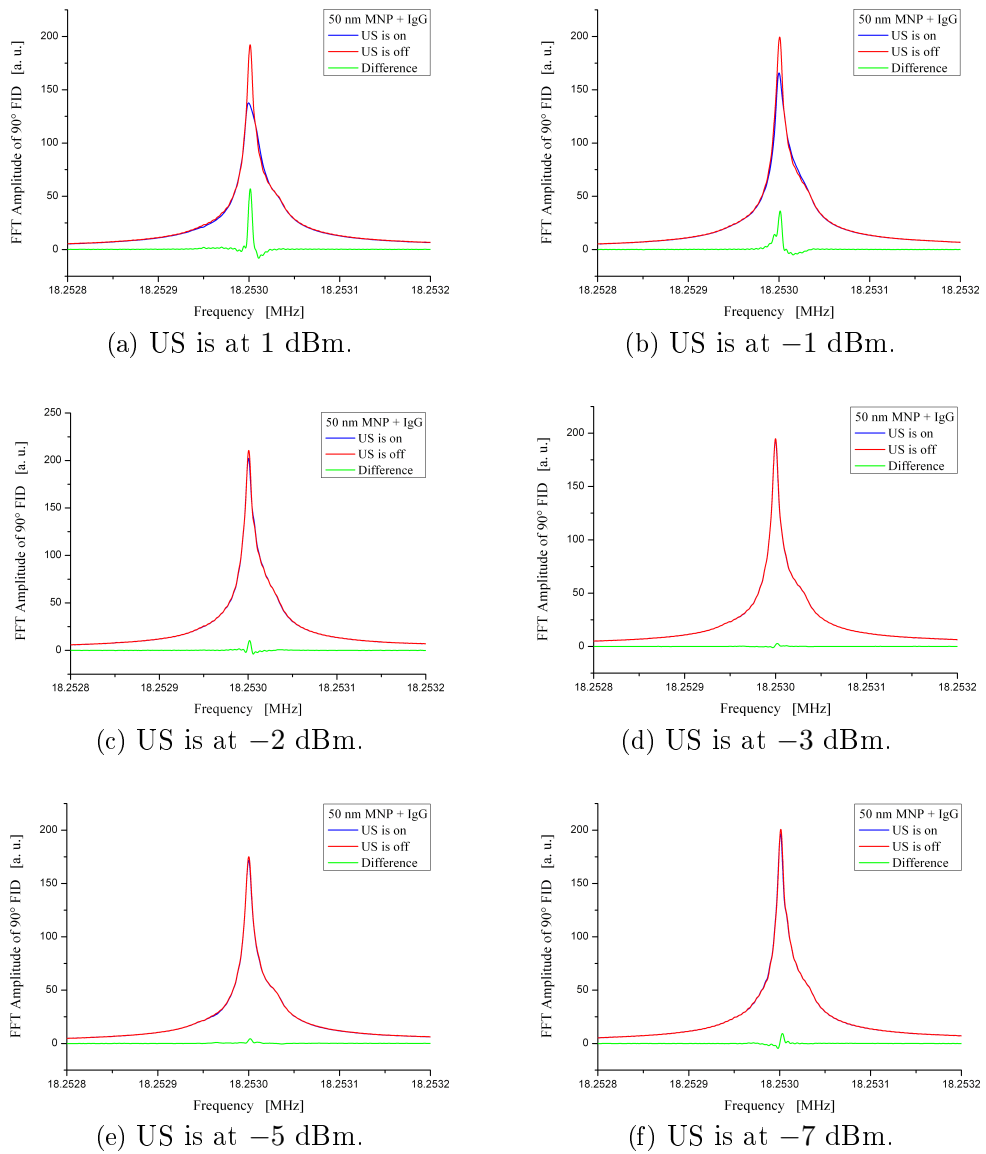


Figure C.1: The FFT amplitudes of the 90° pulse FID for a sample of an aqueous solution with 50 nm MNPs with the IgG antibody attached. The US frequency ν_{US} matched the Larmor frequency ν_0 at 18.253 MHz.

Bibliography

- [1] Bloch, F. Nuclear Induction, *Phys. Rev.*, **75**, 460-474, 1946.
- [2] Purcell, E. M., Torrey, H.C., and Pound, R.V. Resonance absorption by nuclear magnetic moments in solid, *Phys. Rev.*, **69**, 37-38, 1946.
- [3] Al'tshuler, S. A. *Dokl. Akad. Nauk SSSR*, **85**, 1235-1238, 1952.
- [4] Kastler, A. Quelques réflexions à propos des phénomènes de résonance magnétique dans le domaine des radiofréquences, *Experientia*, **8**, 1-9, 1952.
- [5] Bolef, D. I. and Sundfors, R. K. *Nuclear Acoustic Resonance*, (San Diego: Academic Press, Inc.), 1993.
- [6] Proctor, W. G. and Tantilla, W. H. Saturation of Nuclear Electric Quadrupole Energy Levels by Ultrasonic Excitation, *Phys. Rev.*, **98**, 1854, 1955.
- [7] Menes, M. and Bolef, D. I. Observation of Nuclear Resonance Acoustic Absorption of ^{11}In in InSb, *Phys. Rev.*, **109**, 218-219, 1958.
- [8] Gregory, E. H. and Bömmel, H. E. Acoustic Excitation of Nuclear Spin Resonance in Single-Crystal Metallic Tantalum, *Phys. Rev. Lett.*, **15**, 404-406, 1965.
- [9] Bowen, L. O. Nuclear Magnetic Acoustic Resonance in Non-viscous Liquids, *Br. J. Appl. Phys.* **15**, 1451-1452, 1964.
- [10] Bowen, L. O. Nuclear Magnetic Acoustic Resonance and Debye Vibration Potentials in Non-viscous Liquids, *Proc. Phys. Soc.* **87**, 717-720, 1966.
- [11] Homer, J. and Patel, S. U. Preliminary Observations on High-resolution Nuclear Magnetic Resonance for Liquids subjected to Ultrasound, *J. Chem. Soc. Faraday Trans.*, **86**, 215, 1990.
- [12] Vuong, Q. L., Gossuin, Y., and Gillis, P. Acoustical Enhancement of Nuclear Magnetic Relaxation Rates in Liquids, *Phys. Rev. B*, **77**, 212404, 2008.
- [13] Hartman, T. D. *Resonante Ankopplung von Ultraschall an das Kernspinsystem*, Master's Thesis, Rheinische Friedrich-Wilhelms Universität Bonn, 2005.
- [14] Oehms, O. B. *Wechselwirkung des Kernspinsystems mit Ultraschall in einfachen Flüssigkeiten*, Master's Thesis, Rheinische Friedrich-Wilhelms Universität Bonn, 2006.
- [15] Morar, C. *Amplitudenänderung des Kernspinechos durch Ultraschallpulse*, Master's Thesis, Rheinische Friedrich-Wilhelms Universität Bonn, 2006.

- [16] Engelbertz, A. *Variation von NMR-Signalen durch Hyperpolarisation und Ultraschall*, PhD Thesis, Rheinische Friedrich-Wilhelms Universität Bonn, 2007.
- [17] Höhl, C. *Ultraschall in der NMR - Kopplung mit magnetischen Nanopartikeln*, Master's Thesis, Rheinische Friedrich-Wilhelms Universität Bonn, 2007.
- [18] Mende, J. *$^1\text{H-NMR}$ & Resonanter Ultraschall in einem Kolloid aus $\text{Pb}(\text{Ti}, \text{Zr})\text{O}_3$* , Master's Thesis, Rheinische Friedrich-Wilhelms Universität Bonn, 2008.
- [19] Gerlach, W. and Stern, O. Über die Richtungsquantelung im Magnetfeld, *Ann. Physik*, **74**, 673-699, 1924.
- [20] Slichter, C. P. *Principles of Magnetic Resonance* (Berlin: Springer-Verlag), 1989.
- [21] Carrington, A., McLachlan, A.D. *Introduction To Magnetic Resonance* (London: Chapman and Hall), 1967.
- [22] Karshenboim, S. G. and Ivanov, V. G. The g factor of the proton, *Phys. Lett. B*, **566**, 27-34, 2003.
- [23] Bortfeldt, J., and Kramer, B., eds. *Units and Fundamental Constants in Physics and Chemistry*, Subvolume b (New York: Springer-Verlag), 1992.
- [24] Abragam, A. *Principles of Nuclear Magnetism* (Oxford: Oxford University Press), 1961.
- [25] Demtröder, W. *Experimentalphysik 4* (Springer), 1998.
- [26] Fukushima, E., and Roeder, S. B. W. *Experimental Pulse NMR* (Massachusetts: Addison-Wesley Publishing Company, Inc.), 1981.
- [27] Symon, K. R. *Mechanics*, 2nd Edition (Addison-Wesley), 1961.
- [28] Markley, J. L., Horsley, W. J., and Klein, M. P. Spin-Lattice Relaxation Measurements in Slowly Relaxing Complex Spectra, *J. Chem. Phys.*, **55**, 3604-3605, 1971.
- [29] Vold, R. L., Waugh, J. S., Klein, M. P., and Phelps, D. E. Measurement of Spin Relaxation in Complex Systems, *J. Chem. Phys.*, **48**, 3831-3832, 1968.
- [30] Kowalewski, J., and Mäler, L. *Nuclear Spin Relaxation in Liquids: Theory, Experiments, and Applications* (Taylor & Francis Group), 2006.
- [31] Bloembergen, N., Purcell, E. M., and Pound, R. V. Relaxation Effects in Nuclear Magnetic Resonance Absorption, *Phys. Rev.*, **73**, 679-712, 1948.
- [32] Sheard, B., and Bradbury, E. M. Nuclear Magnetic Resonance in the Study of Biopolymers and their Interaction with Ions and Small Molecules, *Prog. Biophys. Molec. Biol.*, **20**, 187-246, 1970.
- [33] Eisinger, J., Shulman, R. G., and Blumberg, W. E. Relaxation enhancement by paramagnetic ion binding in deoxyribonucleic acid solutions, *Nature*, **192**, 963-964, 1961.

- [34] Koenig, S. H., Brown III, R. D. Relaxation of Solvent Protons by Paramagnetic Ions and its Dependence on Magnetic Field and Chemical Environment: Implications for NMR Imaging, *Magn. Reson. Med.*, **1**, 478-495, 1984.
- [35] Renshaw, P. F., Owen, C. S., McLaughlin, A. C., Frey, T. G., Leigh, Jr., J. S. Ferromagnetic Contrast Agents: A New Approach, *Magn. Reson. Med.*, **3**, 217-225, 1986.
- [36] Warren, Jr., W. W., and Wernick, J. H. Nuclear Quadrupolar Relaxation in Solid and Liquid $AuGa_2$, $Au_{0.95}Pd_{0.05}Ga_2$, and $AuIn_2$, *Phys. Rev. B*, **4**, 1401-1405, 1971.
- [37] Hubbard, P. S. Nuclear Magnetic Relaxation of Three and Four Spin Molecules in a Liquid, *Phys. Rev.*, **109**, 1153-1158, 1958.
- [38] Edzes, H. T., and Samulski, E. T. Cross Relaxation and Spin Diffusion in the Proton NMR of Hydrated Collagen, *Nature*, **265**, 521-523, 1977.
- [39] Yanagisawa, M., and Yamamoto, O. Scalar Coupling and Spin-rotation Interactions in the ^{13}C Nuclear Magnetic Relaxation of Methyl- d_3 Bromide, *Bull. Chem. Soc. Jpn.*, **52**, 2147-2148, 1979.
- [40] Vashman, A. A. and Pronin, I. S. Spin-rotation Relaxation of ^{31}P during the Formation of Tributylphosphate Complexes with Nitric Acid, *J. Struct. Chem.*, **13**, 722-724, 1972.
- [41] Leach, M. O. Spatially Localised Nuclear Magnetic Resonance *The Physics of Medical Imaging* ed S Webb (Bristol, UK: Adam Hilger), 1988.
- [42] Browne, M., and Semelka, R. C. *MRI: Basic Principles and Applications* (New York: Wiley), 1999.
- [43] Keller, P. J. *Basic Principles of MR Imaging* (GE Medical Systems), 1991.
- [44] Greenburg, M. D. *Advanced Engineering Mathematics*, Sections 11.3 and 11.4. (Prentice Hall), 1988.
- [45] Hahn, E. L. Spin Echoes, *Phys. Rev.*, **80**, 580-594, 1950.
- [46] Carr, H. Y. and Purcell, E. M. Effects of Diffusion on Free Precession in Nuclear Magnetic Resonance Experiments, *Phys. Rev.*, **94**, 630-638, 1954.
- [47] Haacke, E.M., R.W. Brown, M.R. Thompson, and R. Venkatesan, *Magnetic Resonance Imaging: Physical Principles and Sequence Design*. (New York: John Wiley and Sons), 1999.
- [48] Lauterbur, P. C. Image Formation by Induced Local Interactions: Examples Employing Nuclear Magnetic Resonance, *Nature*, **242**, 190-191, 1973.
- [49] Weinmann, H. J., Brasch, R. C., Press, W. R., and Wesbey GE. Characteristics of Gadolinium-DTPA Complex: A Potential NMR Contrast Agent. *Am. J. Roentgenol.*, **142**, 619-624, 1984.
- [50] Bloch, F., Hansen, W. W., and Packard, M. The Nuclear Induction Experiment. *Phys. Rev.*, **70**, 474-485, 1946.

- [51] Mathur de Vré, R., and Lemort, M. Biophysical Properties and Clinical Applications of Magnetic Resonance Imaging Contrast Agents, *Br. J. Radiol.*, **68**, 225-247, 1995.
- [52] Lauffer, B. R. Paramagnetic Metal Complexes as Water Proton Relaxation Agents for NMR Imaging: Theory and Design, *Chem. Rev.*, **87**, 901-927, 1987.
- [53] Caravan, P., Ellison, J. J., McMurry, T. J., and Lauffer, R. B. Gadolinium(III) Chelates as MRI Contrast Agents: Structure, Dynamics, and Applications, *Chem. Rev.*, **99**, 2293-2352, 1999.
- [54] Koenig, S. H., and Kellar, K. E. Theory of Proton Relaxation in Solutions of Magnetic Nanoparticles, Including the Superparamagnetic Size Range, *Acad. Radiol.*, **3**, Suppl 2, S273-S276, 1996.
- [55] Ohgushi, M., Nagayama, K., and Wada, A. Dextran Magnetite: A New Relaxation Agent and Its Application to T_2 -Measurements in Gel Systems, *J. Magn. Reson.*, **29**, 599-601, 1978.
- [56] M. Helena Mendonca Dias, Paul C. Lauterbur Ferromagnetic particles as contrast agents for magnetic resonance imaging of liver and spleen, *Magn. Reson. Med.*, **3**, 328-330, 1986.
- [57] Gillis, R., and Koenig, S. H. Transverse relaxation of Solvent Protons Induced by Magnetized Spheres: Application to Ferritin, Erythrocytes and Magnetite, *Magn. Reson. Med.*, **5**, 323-345, 1987.
- [58] Fretz, C. J., Elizondo, G., Weissleder, R., Hahn, P. E., Stark, D. D., and Ferrucci, J. T. Superparamagnetic Iron Oxide-Enhanced MR Imaging: Pulse Sequence Optimization for Detection of Liver Cancer, *Radiology*, **172**, 393-397, 1989.
- [59] El'piner, I. E. *ULTRASOUND Physical, Chemical and Biological Effects* (New York: Consultants Bureau), 1964.
- [60] Hill C. R., Bamber, J. C., ter Haar, G. R. (ed), *Physical Principles of Medical Ultrasonics* (Chichester: Ellis Horwood Ltd), 1986.
- [61] Schlengermann, U. *Das Krautkrämer Ultraschall-Taschenbuch* (Krautkrämer GmbH & Co.), 1998.
- [62] Cerdan, S., Lötscher, H. R., Künnecke, B., and Seelig, J. Monoclonal Antibody-Coated Magnetite Particles as Contrast Agents in Magnetic Resonance Imaging of Tumors, *Magn. Reson. Med.*, **12**, 151-163, 1989.
- [63] Morag, E., Bayer, E. A., and Wilchek, M. Reversibility of biotin-binding by selective modification of tyrosine in Avidin, *Biochem.* 316, 193-199 (1996).
- [64] Meinert, L. *Signalerhöhung durch Ultraschall in der Magnetresonanztomographie*, Master's Thesis, Rheinische Friedrich-Wilhelms Universität Bonn, 2007.

Acknowledgment

There are a number of people that directly or indirectly have contributed to the completion of this dissertation.

First of all, I would like to express my sincere gratitude to my supervisor Prof. Dr. Karl Maier for granting me the opportunity to work under his supervision. I thank him for his support, encouragement, and valuable ideas in all matters over the course of this work. I have surely profited from the experience of working under his supervision.

I would like to thank PD Dr. Reiner Vianden, PD Dr. Akaki Rusetsky, and Prof. Dr. Andreas Gansäuer for being interested in my thesis and for kindly accepting to be members of my committee.

I am grateful and highly indebted to my blessed parents for all the care and support I had been provided. I am deeply appreciative to my wife Liela and my children Wajdan, Munib, and Muanas for their love, affection, and patience. Their constant inspiration encouraged me to progress in my work.

I am thankful to my collaborator and my friend Christian Höhl for all his assistance and for having the time to correct my thesis. I really enjoyed working him. I gratefully acknowledge Dr. Klaus Lehnertz for his useful comments.

I would also like to thank my office-mates: Jessica Mende for working together in the NMR laboratory during her diploma and having the time to read my thesis and correct it, Lena Jentjens for working together for the course of the Medical Physics laboratory, and Marcus Radicke for all the good times at the office. I am thankful to Dr. Ole Oehms for working together in the NMR laboratory and for having interesting discussions. I wish him happiness in his married life.

Thanks to Mr. Bernd Habenstein for his valuable advice and delightful conversations. I am also thankful to the Electronic workshop group and the Fine Mechanics workshop group for their assistance. Thanks to my NMR colleagues Peter Wolf, Fahimeh Jahanbakhsh, and Felix Repp for having the time to do the ultrasound power measurements. Also, I would like to thank my NMR ex-colleagues: Dr. Andre Engelbertz, Carmen Morar, Maurice Schlichtenmayer, Sarah Wrede, and Meinert Lewerenz. Thanks to PD Dr. Torsten Staab, Dr. Matz Haaks, Dr. Christine Negrini, and Dr. Poornima Anbalagan. I would like to extend my appreciation to all the members of our group: Patrik Eich, Christian Lenk, Judith Fingerhuth, Iris Kohlbach, Benedikt Klobes, Björn Korff, Osman Balarisi, Anna-Lisa Kofahl, Reinhard Sottong, Niels Raeth, Meng Liu, Judith Schindler, Deniz Ulucay, and ex-colleagues. They have made me feel at home in the working group.

In addition, I am thankful to Mrs. Maier for her kind hospitality and warm welcome at her house. I have been fortunate to share my time at the institute with a great number of people who have assisted me in a way or another in the last few years. Special thanks go

to Ms. Mosblech, Ms. Seifert, Ms. Balci, Ms. Paus, Ms. Hodde, Dr. Mertler, Mr. Wolf, Mr. Hanfland, Mr. Lens, and Mr. Harlow. Also, I would like to thank Teresa Negrini, Makhsud Rasulbaev, Riccardo Valentini, and Michael Steffens.

Finally, on this occasion I would like to express my gratitude and appreciation to my brothers and sisters, my father-in-law, my mother-in-law and all my family members and friends for their continuous support and encouragements. Also, I gratefully acknowledge the Ministry of Higher Education in Libya for sponsoring my Ph.D. studies, and the department of Cultural Affairs in the Libyan Bureau in Berlin for their provision.